

Iron Homeostasis-Regulated Adaptive Metabolism of PEGylated Ultrasmall Iron Oxide Nanoparticles

Ning Wang, Dandan Zhou, Keyang Xu, Dandan Kou, Can Chen, Cang Li, Jianxian Ge, Lei Chen, Jianfeng Zeng,* and Mingyuan Gao*



Cite This: <https://doi.org/10.1021/acsnano.5c01399>



Read Online

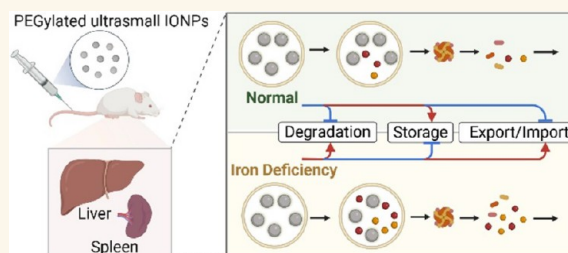
ACCESS |

Metrics & More

Article Recommendations

Supporting Information

ABSTRACT: Iron oxide nanoparticles have become increasingly significant in the biomedical field due to their exceptional magnetic properties and biocompatibility. However, understanding their *in vivo* metabolism and transformation is crucial due to the potential biological effects they may induce. This study investigates the metabolic pathways of PEGylated ultrasmall iron oxide nanoparticles (PUSIONPs) *in vivo*, particularly under varying iron statuses and dosages. Employing a comprehensive analytical approach—including magnetic resonance imaging, elemental analysis, histological assessments, hematological analysis, and Western blot analysis—the biodistribution and transformation of PUSIONPs were mapped. The findings reveal significant differences in the metabolic fate of PUSIONPs between iron-sufficient and iron-deficient conditions, underscoring the pivotal role of iron homeostasis in regulating PUSIONPs biodegradation. In iron-deficient states, degradation and transformation were markedly accelerated, with the released iron rapidly incorporated into hemoglobin. Additionally, the liver and spleen exhibited different PUSIONPs metabolism rates due to their distinct physiological roles: the spleen, primarily responsible for iron recycling, facilitated faster degradation, while the liver, serving as an iron storage organ, showed slower degradation. Under iron deficiency, most degradation products were directed toward hemoglobin synthesis, whereas under normal conditions, the liver gradually metabolized the degradation products, and the spleen retained higher iron levels. Moreover, PUSIONPs degradation demonstrated dose dependency, with higher doses slowing degradation and reducing the utilization rate by the iron-deficient body. Comprehensive safety evaluations confirmed that PUSIONPs exhibit excellent biocompatibility across all doses, with no significant safety concerns. Compared to the clinically used intravenous iron supplement iron sucrose, PUSIONPs also demonstrated superior bioavailability and more effective iron supplementation. These findings provide critical insights into the interaction between iron oxide nanoparticles and iron metabolism, offering a foundation for future research and the broader application of PUSIONPs in biomedical contexts.



KEYWORDS: iron oxide nanoparticle, iron homeostasis, biodegradation, iron deficiency anemia, nanoparticle metabolism

1. INTRODUCTION

The rapid advancements in nanotechnology have positioned iron oxide nanoparticles (IONPs) as one of the most extensively studied nanomaterials. Renowned for their exceptional magnetic properties, IONPs are widely utilized in various biomedical applications, including magnetic resonance imaging (MRI),¹ drug delivery² and magnetic hyperthermia.³ Moreover, IONPs have demonstrated significant biocompatibility when integrated into iron metabolism as intravenous iron supplements.⁴ However, the potential of IONPs to generate free radicals due to excess iron raises concerns about adverse biological effects, while also presenting opportunities for use in antibacterial⁵ and anticancer therapy.⁶ The dual potential

highlights the importance for a thorough understanding of the *in vivo* metabolism of IONPs to maximize their benefits while minimizing potential risks, thereby ensuring their safe and effective use in clinical settings.

Iron, as a transition metal, plays a pivotal role in essential biological processes, including oxygen transport, DNA syn-

Received: January 22, 2025

Revised: March 15, 2025

Accepted: March 17, 2025

thesis, nucleic acid repair, mitochondrial cellular respiration, and cell growth.^{7,8} Under physiological conditions, iron fluctuates between different oxidative states. Ferric (III) iron, although stable, is poorly soluble in water, necessitating the involvement of proteins such as transferrin to facilitate its transport. Conversely, ferrous (II) iron is water-soluble and highly reactive, capable of producing reactive oxygen species (ROS) through the Fenton reaction, potentially leading to cellular damage and organ failure, particularly in vital organs like the liver, heart, pancreas, thyroid, and central nervous system.^{9,10} Excessive iron accumulation can also trigger ferroptosis, a form of iron-dependent cell death characterized by oxidative stress and lipid peroxidation, ultimately leading to membrane damage and cell death.^{11–13} Thus, maintaining iron's indispensable functions while minimizing its harmful potential requires the precise regulation of its uptake, distribution, and utilization.¹⁴ The introduction of exogenous IONPs into the body raises critical questions regarding their impact on iron homeostasis.

Over the past decades, numerous studies have focused on understanding the fate of IONPs *in vivo*. Radioactive labeling studies have demonstrated that ⁵⁹Fe released from IONPs is incorporated into the hemoglobin within 1 week, confirming the integration of IONPs into physiological pathways.^{15,16} Additionally, the degradation of IONPs in the liver and spleen over several months, along with increased levels of endogenous ferritin-bound iron, underscores their potential impact on iron metabolism.^{17–19} Changes in the expression of genes and proteins related to iron metabolism have also been observed following IONP internalization.^{20–22} However, the specific mechanisms through which iron metabolism influences the behavior of IONPs *in vivo* remain poorly understood.

At the cellular level, iron regulatory proteins (IRPs) monitor cytosolic iron concentrations and interact with iron-responsive elements (IRE) to regulate the expression of proteins involved in iron metabolism, such as ferritin and transferrin receptors (TFR),^{23,24} thereby maintaining iron homeostasis. Systemically, the hepcidin/ferroportin (FPN, also known as iron transporter 1 or Ferroportin 1) axis plays a central role in governing iron regulation.²⁵ Hepcidin binds to ferroportin, inducing its internalization and degradation, which in turn regulates iron export from cells.²⁶ Disruptions in iron homeostasis can lead to conditions such as iron deficiency or overload, which are associated with numerous diseases affecting over 2 billion people globally.^{27,28} Despite the critical importance of iron regulation, the impact of iron homeostasis on IONPs metabolism remains unclear. Therefore, investigating IONPs metabolism, particularly under conditions of deregulated iron levels, is essential.

In general, the dosage of IONPs varies significantly depending on their diagnostic and therapeutic applications. Clinical doses of IONPs used as MRI contrast agents typically range below 5 mg/kg,^{29–32} while doses for treating iron deficiency anemia (IDA) can reach approximately 20 mg/kg.⁴ Previous studies have shown that the blood half-life ($t_{1/2}$) of IONPs is highly dose-dependent, with higher doses resulting in prolonged circulation times and altered biodistribution.³³ Additionally, when administered in high dosages, liver and spleen macrophages can only clear a portion of the IONPs from the bloodstream, resulting in the excess IONPs accumulating in other macrophage-rich tissues, such as the lung and adipose tissue.¹⁸ These findings indicate that the dosage of IONPs significantly influences their circulation time

and biodistribution in the body. However, the long-term metabolism and transformation of IONPs at varying dosages have not been systematically studied, which is critical for ensuring their safe application *in vivo*.

To address these issues, PEGylated ultrasmall IONPs (PUSIONPs) with an average size of 3.6 ± 0.4 nm, recognized as one of the most promising next-generation MRI contrast agents, were selected for their exceptional MRI performance to visualize the metabolic process. PUSIONPs were administered under both normal and iron-deficient conditions to evaluate their distribution, degradation, transformation, and excretion, thereby revealing metabolism pattern regulated by iron homeostasis. Furthermore, considering the extensive application of IONPs in diagnostics and therapeutics, the metabolism of PUSIONPs at varying dosages was also studied to understand the dose-dependent effects on their metabolic behavior. Additionally, a comparative study was performed to evaluate the efficacy of PUSIONPs against conventional iron supplements, such as iron sucrose, in treating iron deficiency anemia. This comprehensive study aims to elucidate the impact of iron homeostasis and dosage on PUSIONPs metabolism and provide insights for their safe and effective use in clinical settings.

2. RESULTS AND DISCUSSION

2.1. Characterization of PUSIONPs. The PUSIONPs used in this study were provided by Suzhou Xinying Biomedical Technology Co., Ltd. These nanoparticles consist of an iron oxide core with a magnetite structure,³⁴ coated with a poly(ethylene glycol) (PEG) ligand bearing diphosphonate and methoxyl groups on opposite sides (denoted as DP-PEG).³⁵ Transmission electron microscopy (TEM) image (Figure S1a) revealed that PUSIONPs possess a semispherical morphology with an average core diameter of 3.6 ± 0.4 nm (Figure S1b). Dynamic light scattering (DLS) results (Figure S1c) further indicate that PUSIONPs have an average hydrodynamic diameter of 10.9 nm, confirming that the PEG coating endows the particles with excellent water solubility and effectively prevents aggregation. Additionally, PUSIONPs exhibited a slightly negative surface charge.³⁶ To assess the MRI contrast enhancement capabilities of PUSIONPs, relaxivity measurements were conducted using a preclinical 3T MRI scanner. The longitudinal relaxivity (r_1) and transverse relaxivity (r_2) were determined to be 6.1 and 35.5 $\text{mM}^{-1} \text{s}^{-1}$, respectively (Figure S1d), highlighting their exceptional potential for T1/T2 dual-modal MRI applications.

Compared to larger iron oxide nanoparticles, PUSIONPs offer distinct advantages due to their ultrasmall size and tailored surface properties. The sub-5 nm core size not only enhances their T1-weighted MRI contrast, making them a promising alternative to gadolinium-based contrast agents, but also prolongs their blood circulation time by reducing rapid clearance via the mononuclear phagocyte system.³⁷ Additionally, the synthesis of PUSIONPs via high-temperature thermal decomposition ensures high crystallinity, which enhances their structural stability and minimizes unwanted iron ion leakage, thereby reducing the risk of hypersensitivity and toxicity.^{38,39} The PEGylation of PUSIONPs also contributes to their excellent colloidal stability and antifouling properties, further improving their biocompatibility.⁴⁰ These unique physico-chemical characteristics position PUSIONPs as a promising next-generation platform for biomedical applications, partic-

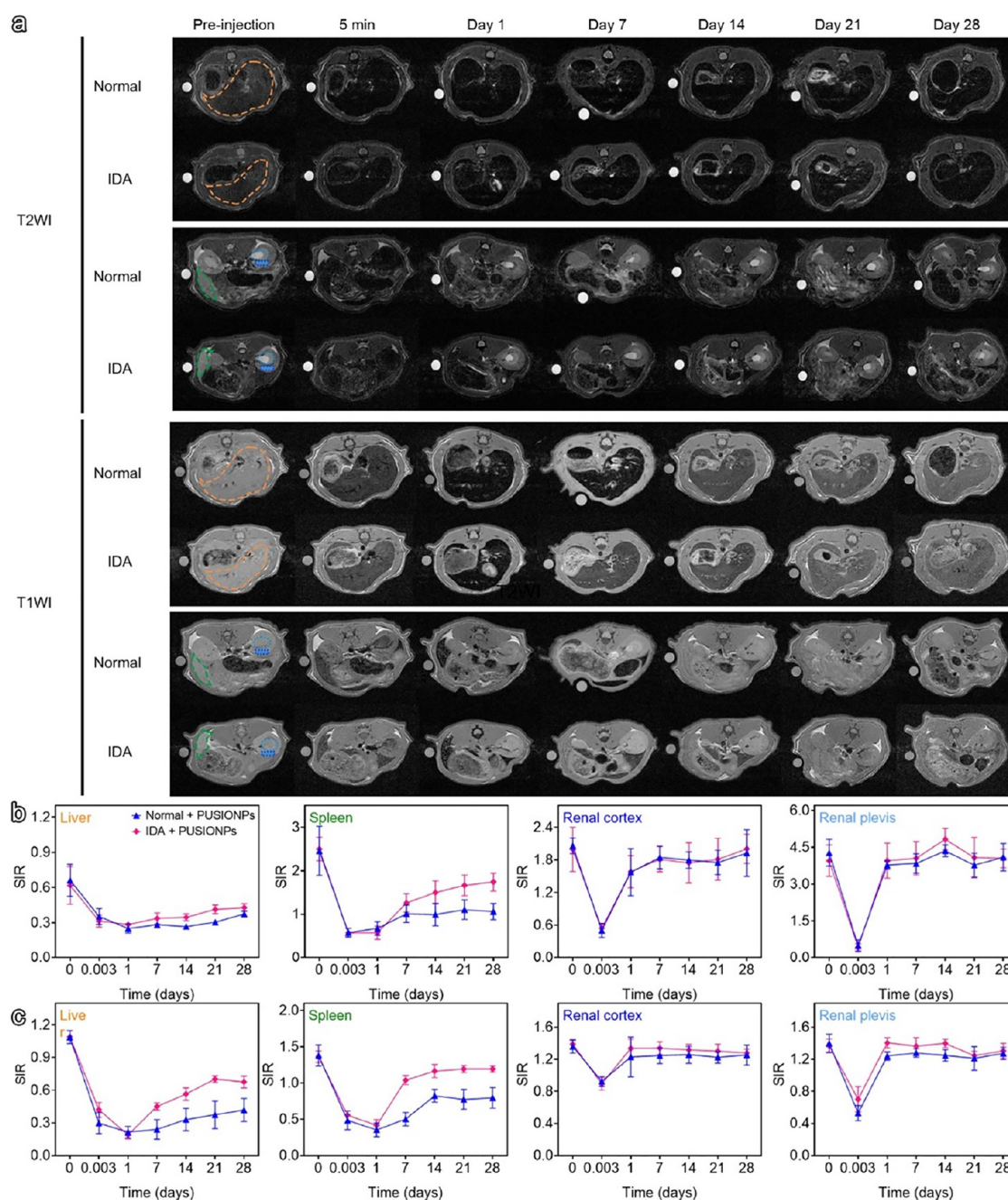


Figure 1. Noninvasive measurement of PUSIONPs biodistribution in normal and IDA rats using MRI. (a) Representative T2-weighted and T1-weighted MR images captured at various time points before and after intravenous administration of PUSIONPs. (b) T2-weighted and (c) T1-weighted signal intensity ratio (SIR) changes over time in different organs, including the liver, spleen, renal cortex, and renal pelvis. Data are presented as mean \pm SD, $n = 4$ rats per group.

ularly in iron metabolism-related disorders and advanced imaging techniques.

2.2. Tracking PUSIONPs *In Vivo* via MRI. To investigate the effect of iron homeostasis on the metabolism of PUSIONPs, IDA model was established on Sprague–Dawley (SD) rats through a combination of a low-iron diet and induced blood loss.⁴¹ Hemoglobin (HGB), mean corpuscular hemoglobin (MCH), and mean corpuscular volume (MCV) levels significantly reduced in the IDA group after 21 days compared to the normal group, confirming the successful induction of IDA (Figure S2). PUSIONPs were then intravenously injected at 20 mg/kg body weight into both

IDA and normal rats, and their biodistribution was monitored using MRI.

It is well established that intravenously administered nanoparticles are primarily sequestered by the liver and spleen, key components of the mononuclear phagocytic system.^{42,43} Furthermore, the kidneys contribute to the clearance of ultrasmall nanoparticles with hydrodynamic diameters below approximately 6 nm.⁴⁴ Therefore, MRI scans were performed for up to 28 days postadministration to track PUSIONPs metabolism in the liver, spleen, and kidneys, taking advantage of their superparamagnetic properties.

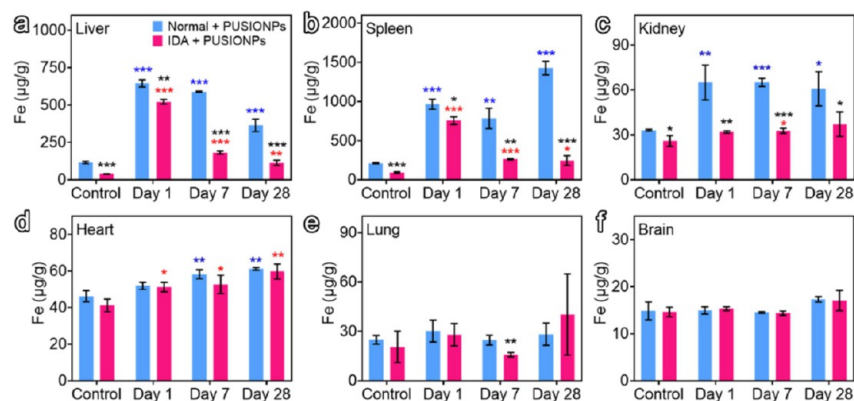


Figure 2. Quantification of iron content in main organs at different time points following PUSIONPs injection. Iron concentration of (a) liver, (b) spleen, (c) kidney, (d) heart, (e) lung, and (f) brain is expressed per mass of fresh organ, $n = 4$ rats per group. Data are presented as mean \pm SD. Significance is indicated as follows: * $P < 0.05$; ** $P < 0.01$; *** $P < 0.001$. Blue and red stars indicate significance when comparing each time point to the control group within the normal and IDA groups, respectively. Black stars indicate significance when comparing normal and IDA groups at each time point.

Figure 1a shows T2-weighted (T2W) and T1-weighted (T1W) MR images acquired preinjection and at various postinjection time points. In T2W MR images, the liver exhibited low baseline signals due to its high endogenous iron content. Immediately after injection, the liver signal further darkened, reflecting rapid uptake of PUSIONPs, and this signal remained consistently low up to 28 days postinjection. In contrast, the T1W images exhibited more dynamic signal variations, with a sharp postinjection decrease reaching its lowest point at day 1, followed by a gradual recovery, suggesting PUSIONPs degradation or clearance. Notably, signal recovery in IDA rats was faster and more pronounced than in normal rats. A similar trend was observed in the spleen, where T2W signals initially decreased before gradually recovering. However, signal recovery in the spleen occurred more rapidly than in the liver, particularly in IDA rats. In contrast, kidney signals exhibited only transient decreases in both T2W and T1W images, with no significant differences between IDA and normal rats.

To further quantify these observations, a quantitative analysis of MR signal intensity (SI) was conducted in various regions of interest (ROIs) (Figure S3). The signals were normalized against muscle signals from the same imaging plane to minimize intermachine variability and enhance reproducibility.⁴⁵ The resulting signal intensity ratios (SIRs) are presented in Figure 1b,c. In the liver, while T2W images showed minimal visible changes postinjection, quantitative analysis revealed a slow recovery trend from day 14 onward, with signals remaining significantly lower than preinjection levels at day 28. In the spleen, T2 signals recovered more quickly, stabilizing by day 7. The faster recovery of MRI signals in both organs in IDA rats suggests that iron deficiency accelerates PUSIONPs degradation and clearance. By day 28, the spleen T2 signal in IDA rats had returned to preinjection levels, indicating near-complete degradation or clearance of PUSIONPs from this organ. In contrast, kidney signals in both the renal cortex and pelvis returned to baseline within 1 day, suggesting minimal long-term retention of PUSIONPs.

The T2* imaging technique is also widely employed for tracking the *in vivo* distribution of magnetic nanoparticles, as it is highly sensitive to local magnetic field changes and particularly valuable for assessing iron deposition. Figure S4 presents the T2* times for different ROIs at various time

points postinjection. Due to the high PUSIONPs concentration, T2* imaging failed to accurately detect liver and spleen signals within the first day postinjection as T2* times were extremely short. However, as time progressed, the T2* times in the liver and spleen gradually increased, reflecting the gradual degradation or clearance of PUSIONPs from these organs. In the kidneys, T2* times returned to near-normal levels within 1 day, further confirming minimal PUSIONPs retention in this organ.

In general, traditional large-sized IONPs, due to their larger magnetic moments, are typically tracked using T2 and T2* imaging techniques. Negative T2 and T2* contrast is usually detectable even at low IONPs concentrations.⁴⁶ However, for applications requiring higher IONPs concentrations for imaging or therapy, conventional T2 and T2*-weighted MRI may not effectively quantify these signals.^{47,48} In contrast, PUSIONPs exhibit excellent T1 relaxation properties, making T1 imaging a superior method for tracking their *in vivo* metabolism. T1 imaging provides a broader dynamic response range, allowing for better monitoring of metabolic processes in high-uptake organs such as the liver and spleen, even at early postinjection stages.

2.3. Monitoring PUSIONPs *In Vivo* via Elemental Analysis. While MRI enables real-time monitoring of signal changes across various organs within the same organism, offering valuable insight into the distribution and metabolism of PUSIONPs, quantifying these processes through MRI poses significant challenges. This difficulty arises because MRI relaxivity is highly sensitive to the local environment and the physical state of PUSIONPs, both of which can change as the nanoparticles degrade and transform within the body.^{49,50} Additionally, although sustained changes in MR images may indicate the persistent presence of the superparamagnetic core, the gradual recovery of these images over time suggests a decrease in the amount of the core within the targeted regions, likely due to either the transformation or direct elimination of PUSIONPs. To distinguish between these possibilities, inductively coupled plasma optical emission spectroscopy (ICP-OES) was utilized to measure the total iron content in extracted organs at various time points following PUSIONPs injection.

As illustrated in Figure 2a, the liver, as the primary iron storage organ, exhibited significantly lower iron content in IDA

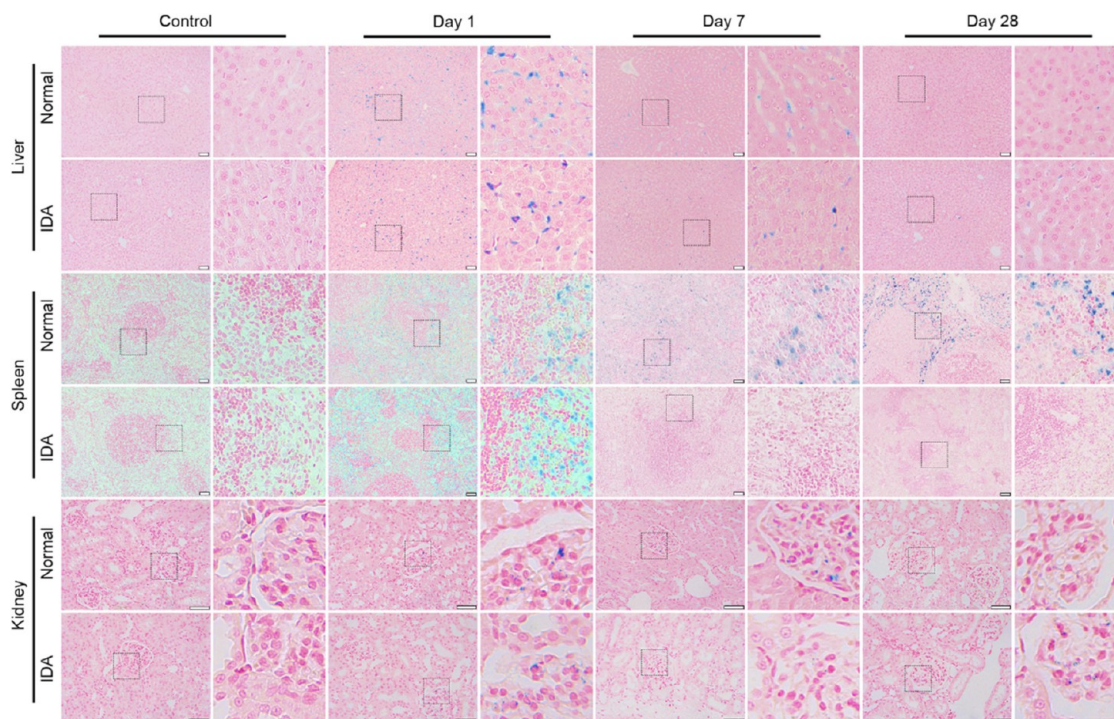


Figure 3. Representative histological images of liver, spleen, and kidney at various time points after PUSIONPs injection. Iron localization appears as blue dots due to the Prussian blue staining. Scale bars correspond to 50 μm .

model rats compared to normal rats due to iron deficiency. Following the injection of PUSIONPs, both groups showed a significant increase in liver iron content, reflecting the substantial uptake of PUSIONPs by the liver. Over time, the iron content gradually decreased, indicating that PUSIONPs were metabolized within the liver. This metabolism occurred at a notably faster rate in IDA rats than in normal rats, aligning with the trends observed in the MRI results. However, the correlation between liver iron content and MRI signal intensity across different groups and time points does not consistently show a positive correlation. For instance, at 28 days postinjection, the liver iron content in normal rats was significantly higher than that in IDA rats at 7 days postinjection. Despite this, MRI results indicated a more pronounced signal recovery in normal rats at 28 days—whether assessed through the SIR in T1- or T2-weighted imaging, or T2* time—compared to IDA rats at 7 days. A similar pattern was observed when comparing liver analysis between normal rats at 7 days and IDA rats at 1 day. This phenomenon suggests that significant degradation of PUSIONPs occurred in the liver, with the resulting degradation products being stored in the liver. Consequently, despite the higher iron content, the MRI signal recovery was more pronounced, indicating that the degradation of PUSIONPs plays a crucial role in the observed imaging outcomes.

Similarly, the spleen of IDA rats had significantly lower iron content than that of normal rats (Figure 2b). After the injection of PUSIONPs, the iron content in both groups significantly increased at 1 day postinjection. However, subsequent changes in spleen iron content differed under varying iron homeostasis conditions. In IDA rats, spleen iron content rapidly decreased over time, reaching preinjection levels of normal rats by 7 days, indicating rapid metabolism of PUSIONPs from the spleen, which aligns with the MRI results. In contrast, in normal rats, spleen iron content decreased

slightly at 7 days compared to 1 day, but then increased further at 28 days, suggesting that PUSIONPs metabolism in the spleen is more significantly influenced by iron homeostasis than in the liver. Combined with the MRI results, which showed partial recovery of spleen MRI signals in normal rats within 7 days and stabilization after 14 days, it is inferred that while PUSIONPs were degraded in the spleen, their clearance was limited, with additional iron sources possibly contributing to the increased iron content.

Regarding the kidneys (Figure 2c), the iron content in normal rats showed a slight increase after PUSIONPs injection, although this increase was much lower compared to the liver and spleen. This discrepancy with MRI findings might be attributed to the sensitivity of MRI or the uneven distribution of PUSIONPs within the kidneys. By 28 days, the iron content had decreased compared to levels at 7 days, indicating that iron in the kidneys continues to be metabolized and excreted to maintain iron homeostasis. In IDA rats, kidney iron content gradually increased throughout the study period, eventually reaching levels similar to those observed in normal rats before injection, suggesting that iron deficiency in the kidneys was progressively alleviated following PUSIONPs administration.

For the heart (Figure 2d), iron content increased modestly after PUSIONPs injection in both normal and IDA rats, although this increase was less significant than in the kidneys. After 7 days, iron content gradually decreased, returning to balanced levels. In the lungs and brain (Figure 2e,f), no statistically significant changes in iron content were observed after PUSIONPs administration.

2.4. Prussian Blue Staining Analysis of Different Organ Sections. To gain a deeper understanding of the metabolism process of PUSIONPs, Prussian blue staining was performed on tissue sections from various organs to visualize the distribution of PUSIONPs at both the tissue and cellular levels, as illustrated in Figures 3 and S5. On day 1

Table 1. Distribution of Injected Iron Dose (% ID) across Various Organs in Normal and IDA Rats at Different Time Points Following PUSIONPs Injection^a

organ	normal + PUSIONPs			IDA + PUSIONPs		
	day 1	day 7	day 28	day 1	day 7	day 28
liver	83.3 ± 2.9	73.4 ± 9.4	37.3 ± 5.1	67.4 ± 7.0	30.7 ± 7.1	9.7 ± 2.5
spleen	10.0 ± 1.5	5.2 ± 1.9	9.9 ± 4.0	10.5 ± 1.1	1.7 ± 0.5	1.2 ± 0.7
kidneys	1.5 ± 0.4	1.4 ± 0.3	0.7 ± 0.5	0.4 ± 0.0	0.4 ± 0.1	0.5 ± 0.3
lungs	0.7 ± 0.3	0.9 ± 0.7	0.9 ± 0.6	0.5 ± 0.3	/	0.7 ± 0.6
brain	/	/	/	0.1 ± 0.1	/	/
heart	0.2 ± 0.1	0.3 ± 0.1	0.2 ± 0.2	0.1 ± 0.2	0.2 ± 0.1	0.1 ± 0.1
sum	95.4 ± 3.9	84.7 ± 4.1	49.2 ± 6.6	78.9 ± 7.4	32.9 ± 6.8	12.3 ± 3.1

^aData are expressed as mean ± SD for $n = 4$ rats per group. The symbol “/” indicates that the concentration determined is lower than the control.

postadministration, a substantial amount of staining was observed in the liver, with the intensity gradually decreasing from the portal areas toward the central veins of the lobules. Given that blood from both the hepatic artery and portal vein mixes within the hepatic sinusoids and drains through the central vein,^{51,52} this pattern suggests that after entering the liver, PUSIONPs traveled along the sinusoids, interacting with various cells along this pathway. Consequently, there was a higher accumulation of nanoparticles in cells located near the blood vessel entry points compared to those near the exit points. Additionally, the staining was predominantly observed in endothelial cells (red arrows), Kupffer cells (blue arrows), hepatocytes (black arrows) (Figure S6), which is consistent with our previous findings.⁴⁴

By day 7 postadministration, Prussian blue staining in liver sections had significantly diminished in both IDA and normal rats. However, ICP analysis revealed that the overall iron levels in the liver of normal rats had not decreased significantly compared to day 1. This discrepancy suggests that by this time, PUSIONPs had undergone substantial degradation within the liver, with the resulting degradation products, such as ferritin, being more widely and uniformly dispersed at both the tissue and cellular levels. After degradation, the local iron concentration was significantly decreased compared to the initial stage postinjection, where PUSIONPs were confined within the endosomes of various liver cells.³⁶ This reduction in local concentration likely accounts for the diminished Prussian blue staining, despite the overall iron concentration remaining comparable. This observation aligns with our previous *in vitro* degradation studies, which demonstrated that most PUSIONPs degraded within 3 days when exposed to a continuous flow of lysosomal-simulated fluid.⁵³ By day 28 postinjection, only a small amount of staining was observed in hepatocytes in both IDA and normal rats, despite the liver iron concentration in normal rats remaining relatively high. This indicates that by this stage, the PUSIONPs had largely degraded and were stored as ferritin within the liver. Furthermore, a comparison of staining patterns between normal and IDA rats over time revealed similar trends, suggesting that the degradation behavior of PUSIONPs was not significantly influenced by iron status. However, the faster decline in liver iron levels observed in IDA rats might be attributed to the more rapid transport of ferritin-bound degradation products out of the liver.

In spleen sections, significant Prussian blue staining was observed on day 1 postadministration in the red pulp and marginal zones of both normal and IDA rats, indicating that PUSIONPs were primarily phagocytosed by macrophages in these regions. By day 7, staining had largely disappeared in

IDA rats, suggesting that PUSIONPs had been substantially metabolized and cleared from the spleen, consistent with the MRI and ICP results. However, in normal rats, noticeable staining persisted in spleen sections even at day 28. Combined the MRI and ICP analysis results, this finding suggests that while PUSIONPs in the spleen underwent degradation, they were not efficiently metabolized or excreted. Unlike in the liver, where degradation products were widely dispersed and thus not readily stained, the persistence of staining in the spleen may be attributed to the distinct cellular distribution of PUSIONPs. In the spleen, PUSIONPs were concentrated within a smaller population of macrophages,⁵⁴ resulting in a higher local concentration even after degradation. This concentration remained sufficient for detection by Prussian blue staining.

In kidney sections, Prussian blue staining was observed in the glomeruli on day 1 postadministration, likely due to the retention or filtration of PUSIONPs in the glomerular capillaries after passing through the afferent arterioles. This retention led to an increase in iron content within the kidneys (Figure 2c) and subsequent staining of the glomeruli. However, the overall MRI signal of the kidneys did not show significant changes compared to preadministration levels on day 1, possibly due to the uneven distribution of PUSIONPs, which were largely confined to the glomeruli—a structure that represents only a small portion of the total kidney volume. Over time, the intensity of the staining gradually decreased, although some residual staining remained visible even at day 28.

In contrast, no significant staining was observed in the heart, lungs, or brain sections, consistent with the ICP results, which showed minimal distribution of PUSIONPs in these organs (Figure S5).

2.5. Biodistribution and Transformation of PUSIONPs

In Vivo. To further investigate the *in vivo* metabolic behavior of PUSIONPs, we analyzed their distribution across different organs at various time points postadministration, as summarized in Table 1. On day 1 postinjection, PUSIONPs predominantly accumulated in the liver and spleen. Although the iron concentration in the spleen was significantly higher than in the liver (Figure 2), due to the smaller mass of the spleen, the liver served as the primary reservoir for PUSIONPs, followed by the spleen. The distribution patterns observed across various organs over time corresponded closely with the changes in iron concentration within these tissues. In IDA rats, the rate of decline in PUSIONPs levels within the liver and spleen was faster than in normal rats. Moreover, in normal rats, the amount of PUSIONPs in the spleen at day 28 was higher than at day 7. Notably, on day 1 postinjection, up to 95.4% of

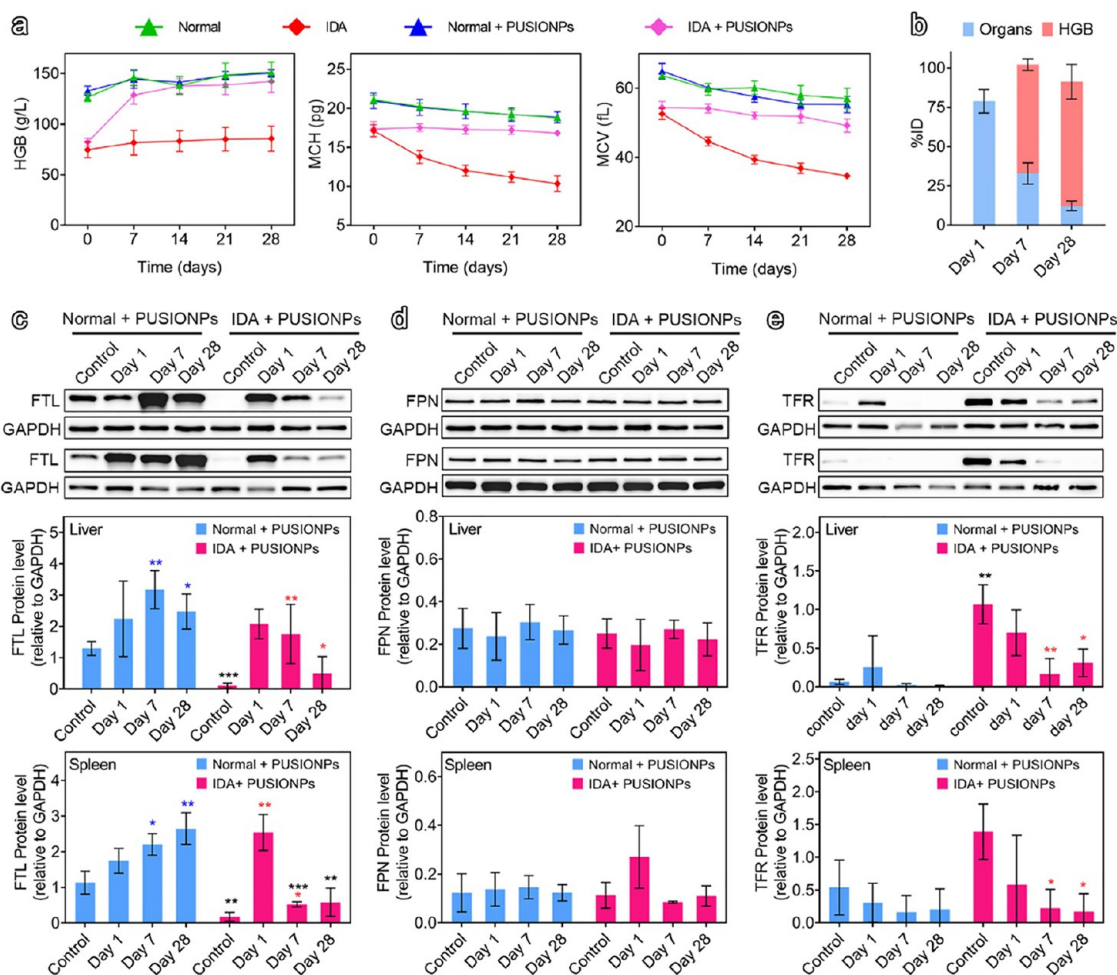


Figure 4. Transformation of PUSIONPs *in vivo*. (a) Changes of HGB, MCH, and MCV at various time points after PUSIONPs injection, $n = 4$ rats. (b) Iron accumulation in HGB and major organs after PUSIONPs injection, $n = 4$ rats. Expression of (c) FTL, (d) FPN, (e) TFR in liver and spleen, $n = 3$ rats. Data are presented as mean \pm SD; * $P < 0.05$; ** $P < 0.01$; *** $P < 0.001$. Blue and red stars denote significant differences compared to the control group within normal and IDA groups, respectively, at each time point. Black stars indicate significant differences between the normal and IDA groups at each time point.

the PUSIONPs were localized within the major organs in normal rats, whereas this percentage was reduced to 78.9% in IDA rats. By day 28, nearly half (49.2%) of the injected iron still remained within these major organs in normal rats, compared to only 12.3% in IDA rats. These findings indicate that PUSIONPs were metabolized more rapidly in iron-deficient conditions.

Typically, iron is metabolized and continuously redistributed in the body through complex regulatory mechanisms, with approximately 70% of iron bound to HGB and around 20% stored in ferritin.⁵⁵ To further investigate the fate of iron after its reduction in the organs, we monitored HGB levels in the rats postadministration, as depicted in Figure 4a. The results showed no significant difference in HGB levels between the treated and control groups in normal rats, indicating that the normal physiological regulation of exogenous iron prevents it from significantly affecting erythropoiesis. However, in IDA rats, HGB levels significantly increased after 7 days of treatment compared to the IDA control group, reaching levels similar to those in normal rats by day 14. Additionally, MCH and MCV were significantly higher in the treated IDA group, indicating a notable improvement in iron deficiency anemia symptoms. Further calculations revealed that by day 7, a

substantial portion of the PUSIONPs degraded in IDA rats, with 69.3% of the released iron being utilized for HGB synthesis. By day 28, this proportion had increased to 79.1%. Figure 4b summarizes the residual iron levels in various organs and the iron that had entered the bloodstream in IDA rats. The data indicate that over 90% of the injected PUSIONPs remained in the body, with most of the iron being effectively utilized.

Moreover, on day 1 postinjection, the cumulative iron content in the organs of IDA rats accounted for only 78.9% of the administered dose, with no observed change in HGB levels (Figure S7a). This suggests that approximately 20% of the iron had already entered the hematopoietic system but had not yet been incorporated into HGB, as erythropoiesis requires time. To further investigate this process, reticulocyte hemoglobin equivalent (RET-He) was evaluated to assess the most recent status of HGB synthesis.⁵⁶ Figure S7b shows a rapid increase in RET-He within 3 days, followed by a decline at 7 days, indicating that the majority of PUSIONPs were degraded and utilized within this period. Simultaneously, HGB levels increased by day 3 and reached a higher level by day 7 postinjection (Figure S7a). Generally, after HGB production in the bone marrow, reticulocytes are released into peripheral

blood 2–3 days later and differentiate into mature red blood cells within 1–2 days.⁵⁷ Therefore, the observed changes are consistent with HGB production and further confirm the rapid degradation of PUSIONPs within 1 day in IDA rats.

Analysis of the data from Table 1 and Figure 4b suggests that in normal rats, the iron reduced in the organs did not enter the bloodstream, indicating that the degraded PUSIONPs were not utilized by the body but were gradually excreted. To investigate this further, the iron content in the feces and urine collected postadministration was measured, as shown in Figure S8. The results indicated that only a small fraction (<1%) of PUSIONPs were excreted via urine within 4 h postinjection, while the remainder entered the organs for subsequent transformation and metabolism. However, due to the high iron content in the diet of normal rats, iron measurements in the feces were confounded, preventing the collection of useful data. Although IDA rats were fed an iron-deficient diet, only a slight difference in fecal iron content was observed between the treatment and control groups. Trace amounts of dietary iron still interfered with the measurements, making it difficult to draw accurate conclusions. Nonetheless, by day 7, PUSIONPs in the liver of normal rats had significantly degraded, as previously mentioned. Therefore, it is hypothesized that in normal rats, although the possibility that some PUSIONPs were excreted in their original particle form via the hepatobiliary route cannot be ruled out, it is more likely that the majority of PUSIONPs were gradually excreted after degradation through the body's normal iron metabolism pathways.

2.6. Transformation Mechanism of PUSIONPs *In Vivo*.

Iron metabolism in the body is closely regulated by key iron-related proteins, primarily ferritin, FPN and TFR. Ferritin, the primary iron storage protein, is composed of ferritin heavy chains (FTH) and ferritin light chains (FTL), capable of storing up to 4500 Fe³⁺ ions.^{8,58} FTH subunits exhibit ferroxidase activity, converting Fe²⁺ to Fe³⁺ for safe storage within the ferritin mineral core, while FTL subunits, although lacking catalytic activity, facilitate nucleation and mineralization of the iron center.⁵⁹ Under normal physiological conditions, ferritin synthesis is regulated at the translational level in response to iron availability. As intracellular ferritin levels rise, excess Fe²⁺ is oxidized to Fe³⁺ and stored within the protein shell, mitigating the Fenton reaction and reducing ROS production, thereby protecting cells from oxidative stress. FPN, primarily expressed on cell surfaces, regulates the export of iron from cells into the bloodstream, ensuring adequate iron levels throughout the body. TFR, on the other hand, is essential for iron uptake into cells. It binds to transferrin, the primary iron transport protein in blood, facilitating the endocytosis of the transferrin-iron complex and subsequent release of iron within the cells. To gain deeper insights into the *in vivo* transformation of PUSIONPs, the expression levels of ferritin, FPN and TFR were monitored in the liver and spleen at various time points postadministration. Ferritin expression was specifically assessed through the measurement of FTL levels, as depicted in Figure 4c–e.

In IDA rats, severe iron deficiency leads to the binding of IRPs to IREs on ferritin mRNA, preventing its translation and consequently reduces ferritin synthesis. As a result, FTL levels in the liver and spleen of IDA rats were significantly lower compared to those in normal rats. Following the administration of PUSIONPs, the increase in iron levels, due to the degradation of PUSIONPs, inhibited IRP activity, preventing it

from binding to IREs and thereby promoting ferritin synthesis. This led to a substantial rise in ferritin levels in the liver and spleen on day 1 postadministration, as ferritin bound to the iron ions released from degraded PUSIONPs. Subsequently, these stored iron ions were transported into the hematopoietic system for hemoglobin synthesis, causing a decrease in iron levels in the liver and spleen, which in turn led to a downregulation of ferritin expression.^{60,61}

Notably, unlike the gradual decrease in FTL levels observed in the liver, FTL levels in the spleen declined more rapidly, reaching a plateau by day 7. Concurrently, FPN expression in the spleen of IDA rats significantly increased on day 1, but returned to baseline levels by day 7. Given that PUSIONPs degrade more quickly in the spleen than in the liver, these findings suggest that under iron-deficient conditions, PUSIONPs not only degrade rapidly in the spleen but also release iron ions that are swiftly bound to ferritin and transported to the hematopoietic system via FPN. This rapid transport reduces iron levels in the spleen, leading to a subsequent decline in both FTL and FPN levels.

Regarding TFR, its expression levels in the liver and spleen of IDA rats were significantly higher than those in normal rats prior to administration, reflecting the increased need for iron. One day after PUSIONPs administration, TFR expression levels in IDA rats significantly decreased, and by day 7, they had returned to levels comparable to those in normal rats. This indicates that iron levels in liver and spleen cells were rapidly restored, reducing the cells' demand for iron. These findings further suggest that PUSIONPs underwent degradation within 1 day, with the released iron actively contributing to the regulation of the body's iron balance.

In normal rats, FTL expression in the spleen gradually increased after 1 day postadministration, while in the liver, maximum FTL elevation was observed by day 7. This also confirms that by day 7, PUSIONPs in the liver of normal rats had significantly degraded, with the resulting iron ions stored in ferritin and gradually metabolized out of the body, leading to a decrease in FTL levels by day 28. In the spleen, due to the lower demand for iron under normal physiological conditions, most of the iron from degraded PUSIONPs was not transported to the hematopoietic system for hemoglobin synthesis. Additionally, during regular physiological processes, macrophages in the spleen continually phagocytose aging red blood cells and recycle their iron, leading to a gradual increase in ferritin and, consequently, FTL levels in the spleen. This is consistent with earlier ICP results, which showed higher iron content in the spleen at day 28 compared to days 1 and 7. Moreover, FPN and TFR levels in normal rats did not show significant changes compared to FTL, indicating that the degradation of PUSIONPs in the body is more closely associated with ferritin. This correlation is reasonable, as ferritin can be considered a chelating agent that binds to iron ions. Previous *in vitro* degradation experiments demonstrated that the presence of chelating agents significantly accelerated the degradation of PUSIONPs in lysosomal-simulated fluid.⁶² Furthermore, immunohistochemical analysis was performed to visualize the spatial distribution of FTL, FPN, and TFR in the liver and spleen at different time points postadministration (Figures S9 and S10). The results were largely consistent with the Western blot analysis, further supporting the observed trends.

In summary, the results demonstrate that the *in vivo* degradation and transformation of PUSIONPs are closely tied

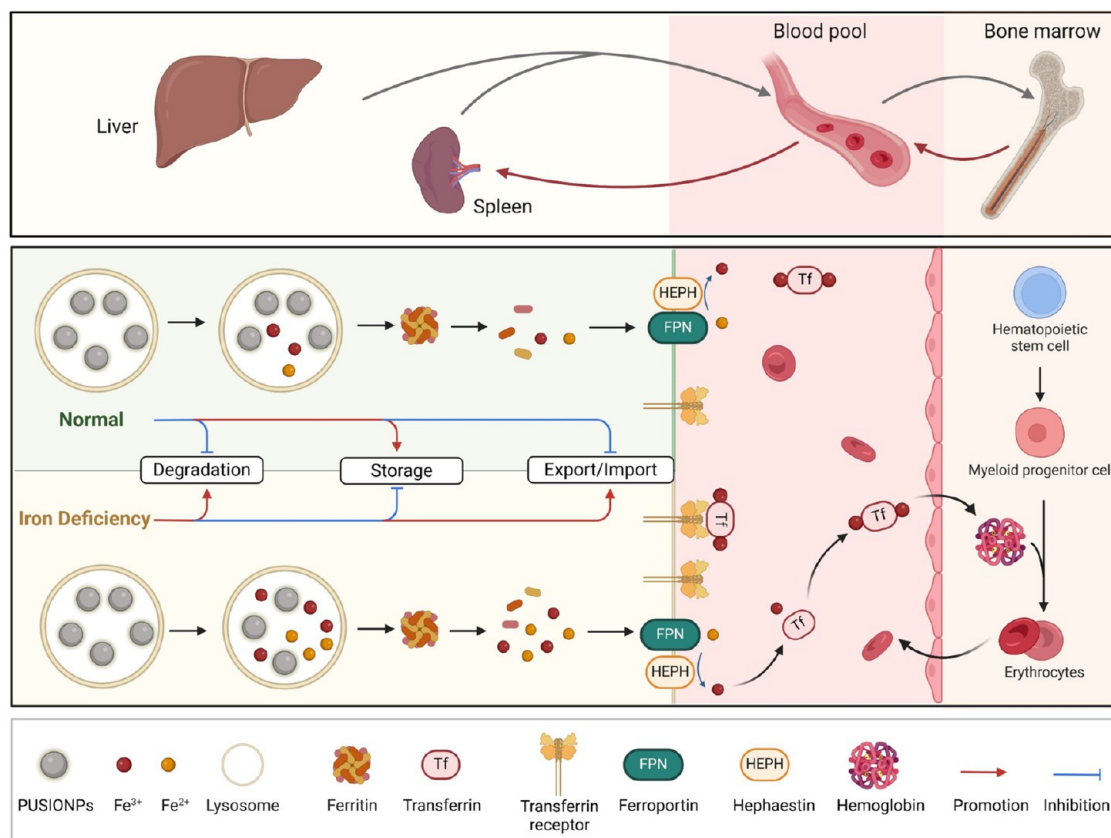


Figure 5. Complete life cycle of PUSIONPs in normal and iron deficiency status.

to iron homeostasis, as illustrated in Figure 5. Under iron-deficient conditions, the body regulates the rapid degradation of PUSIONPs to meet its iron requirements. Furthermore, the degradation and transformation processes of PUSIONPs differ between the spleen and liver due to their distinct functions. The spleen, which plays a crucial role in recycling and utilizing iron, degrades PUSIONPs more rapidly. When the body is iron-deficient, the spleen efficiently transports the degradation products to the hematopoietic system for hemoglobin synthesis. However, in the absence of iron deficiency, these degradation products accumulate in the spleen, along with recycled iron from aging red blood cells, resulting in higher iron levels within the spleen. In contrast, the liver, as an iron storage organ, degrades PUSIONPs at a slower pace but is capable of storing large amounts of ferritin. When iron is needed, the liver gradually transfers ferritin to the hematopoietic system. Conversely, when there is no iron deficiency, the liver metabolizes the excess ferritin out of the body through normal iron metabolism pathways. These findings suggest that compared to the liver, the spleen is more susceptible to the effects of PUSIONPs following intravenous administration and could potentially serve as a target organ for PUSIONPs, warranting further attention in subsequent studies.

2.7. Metabolism of PUSIONPs in Different Doses *In Vivo*. To investigate the impact of dosage on the *in vivo* metabolism of PUSIONPs, three different doses were selected: 10, 20, and 40 mg Fe/kg body weight. After injecting these doses into IDA rats, a comprehensive analysis was conducted to assess the distribution, degradation, and transformation behavior of PUSIONPs at various time points using MRI, ICP, and Prussian blue staining. The T1 and T2-weighted MR

images of the liver, spleen, renal cortex, and pelvis are shown in Figures 6a and S11a, respectively, with corresponding quantitative analyses of the SIR and T2* times provided in Figures 6b, S11b, and S12. As expected, in all groups, MRI signals in the liver and spleen reached their lowest levels at day 1 postinjection. Over time, these signals gradually recovered, with the spleen showing a faster and more pronounced recovery compared to the liver. This pattern indicates that PUSIONPs degrade more rapidly in the spleen than in the liver, regardless of the dose. However, both signal intensity and recovery rate exhibited a dose-dependent relationship within the same organ. Higher doses resulted in lower MRI signals and slower recovery rates, suggesting that the degradation and clearance of PUSIONPs are influenced by dosage, with higher doses potentially saturating the liver and spleen's degradation capacity. Additionally, in the kidneys, MRI signals showed a transient decrease across all doses, returning to baseline levels within 1 day. However, different initial concentrations of PUSIONPs in the bloodstream led to varying SIR values at 5 min postinjection, with higher doses corresponding to lower SIR values due to the higher blood concentrations of PUSIONPs.

To assess the utilization of degraded PUSIONPs by the hematopoietic system, the levels of RET-He, HGB, and MCV were measured at different time points postinjection, as shown in Figure 6c. Across all doses, RET-He levels peaked on day 3, and HGB levels significantly improved by day 3, reaching a plateau by day 7. These findings, in conjunction with the erythrocyte production cycle, further confirm that PUSIONPs undergo rapid degradation within 1 day of administration and subsequently contribute to hemoglobin synthesis. Additionally,

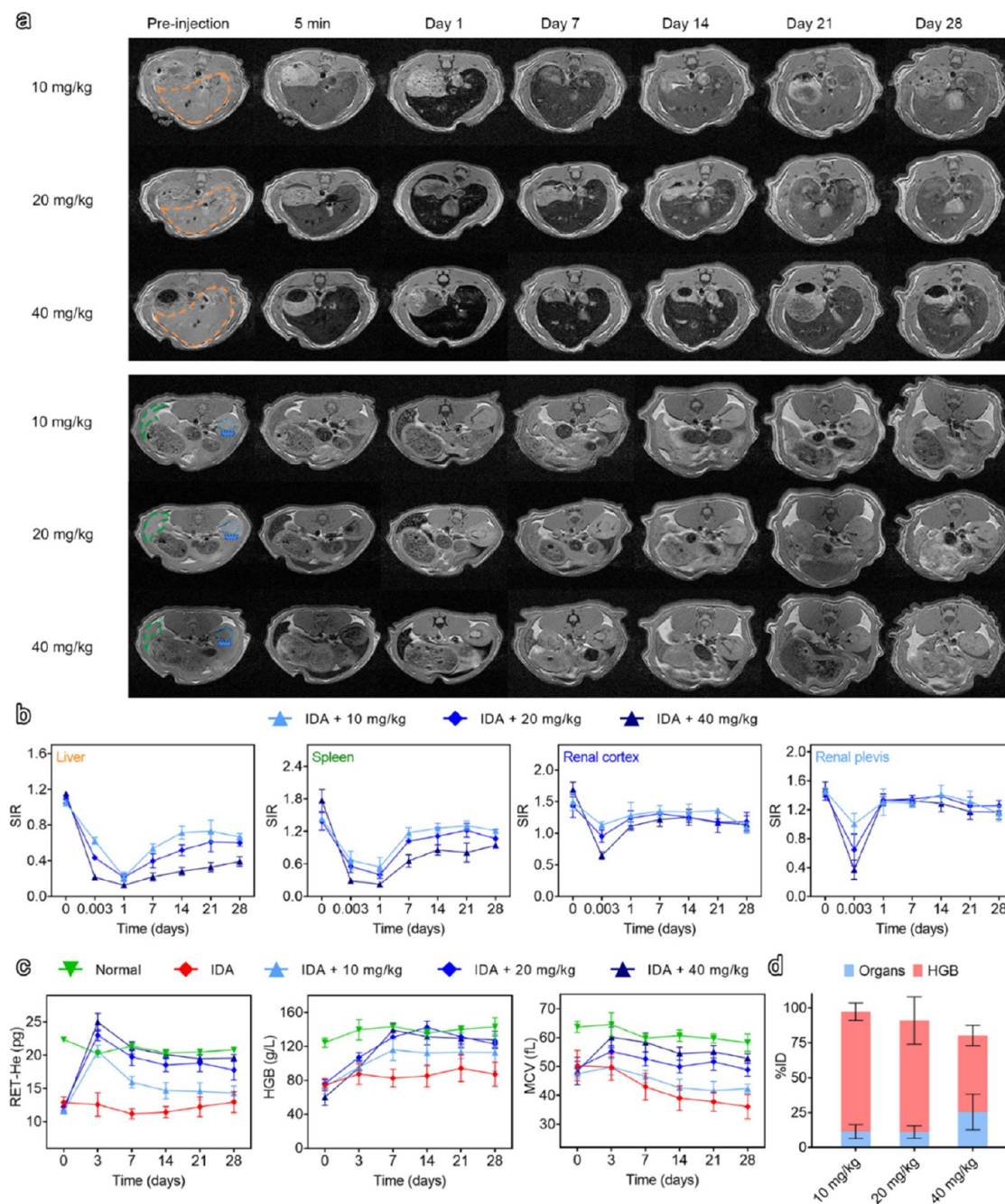


Figure 6. Long-term fate of PUSIONPs at different doses monitored at various time points postinjection. (a) Representative T1-weighted MR images and (b) SIR changes in the liver, spleen, renal cortex, and renal pelvis. (c) Changes in RET-He, HGB, and MCV. (d) Iron accumulation in HGB and major organs 28 days postinjection. Data are presented as mean \pm SD, $n = 4$ rats per group.

the changes in these parameters exhibited a dose-dependent relationship, indicating that the degradation and transformation of iron are influenced by dosage. Higher doses led to increased RET-He and MCV levels, reflecting enhanced initial degradation of PUSIONPs and their subsequent entry into the hematopoietic system. However, it is important to note that while increasing the dose from 10 to 20 mg/kg significantly improved HGB recovery, further increasing the dose to 40 mg/kg did not yield additional HGB recovery. This suggests that under iron-deficient conditions, the body regulates the entry of iron into the hematopoietic system to meet, but not exceed, the demand for hemoglobin synthesis.

Both the 20 and 40 mg/kg doses were sufficient to restore HGB levels to normal in IDA rats.

At 28 days postinjection, a quantitative analysis of iron content in the liver, spleen, kidneys, heart, lungs, and brain was performed, as shown in Figure S13. The iron levels in these organs exhibited a dose-dependent trend. In the 10 and 20 mg/kg groups, the iron concentrations in the organs were only slightly elevated compared to the untreated control group, suggesting that by day 28, PUSIONPs at these doses had largely degraded and metabolized. In contrast, the 40 mg/kg group exhibited significantly higher iron levels, particularly in the liver and spleen, indicating that some PUSIONPs persisted. This was further corroborated by Prussian blue staining of

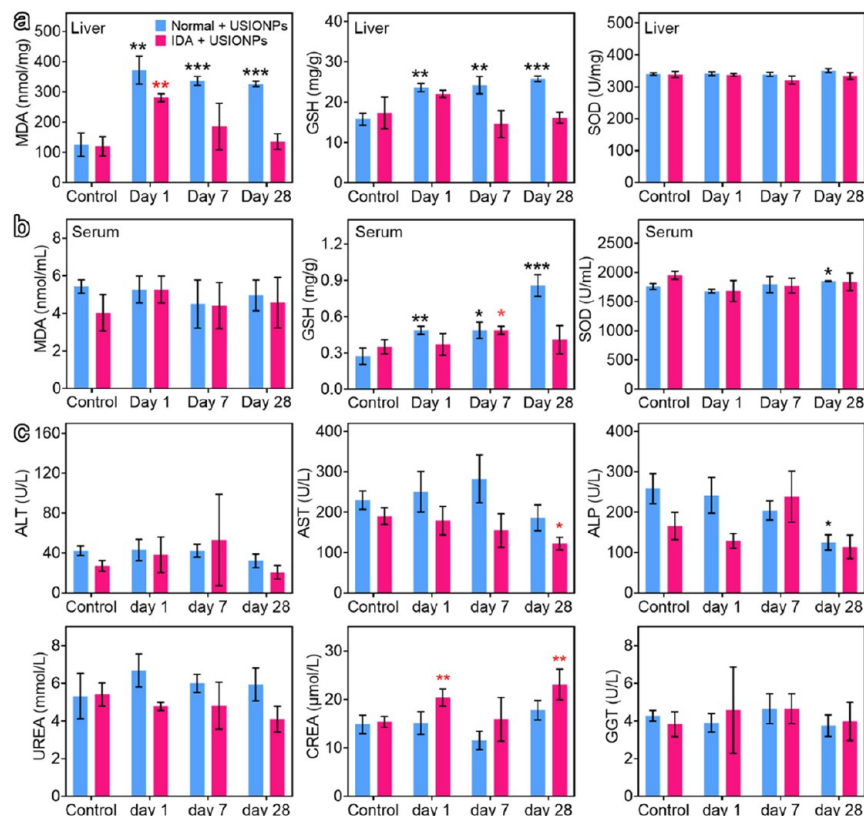


Figure 7. Evaluation of oxidative stress parameters and biochemical markers in liver and serum at various time points after PUSIONPs injection. Oxidative stress markers, including malondialdehyde (MDA), glutathione (GSH), and superoxide dismutase (SOD) levels in (a) liver and (b) serum. (c) Biochemical markers, including alanine aminotransferase (ALT), aspartate aminotransferase (AST), alkaline phosphatase (ALP), urea (UREA), creatinine (CREA), and γ -glutamyl transpeptidase (GGT), were determined at different time points postinjection in both normal and IDA rats. Data are presented as mean \pm SD, $n = 4$ rats per group. Significant differences are indicated by stars, where * $P < 0.05$; ** $P < 0.01$; *** $P < 0.001$. Blue and red stars represent statistical comparisons to the control group in the normal and IDA groups, respectively, while black stars represent comparisons between normal and IDA groups at each time point.

organ sections (Figure S14), which showed no significant staining in the 10 and 20 mg/kg groups, but clear blue staining in the liver and spleen of the 40 mg/kg group. Along with the incomplete recovery of MRI signals in this group, these findings suggest that PUSIONPs accumulated to a certain extent at higher doses. These results align with the *in vitro* model, where a reservoir of intact nanoparticles coexists with rapidly degrading nanocrystals.⁶³ Considering the differences in degradation and transformation between normal and IDA conditions, these findings further elucidate the regulatory mechanisms governing PUSIONPs degradation *in vivo*. The body continuously assesses iron homeostasis, adjusting the degradation and transformation of PUSIONPs accordingly; when PUSIONPs exceed the required amount, their degradation and transportation slows, with the resulting ferritin stored in the liver and spleen, gradually integrating into the body's iron metabolism processes.

Additionally, the distribution of PUSIONPs across various organs at 28 days postinjection was calculated for each dose, as presented in Table S1. The results indicated that the total iron content distributed among the organs increased with the dosage, primarily due to elevated iron levels in the liver at higher doses. By summing the remaining iron in the organs with the iron incorporated into hemoglobin, the data were compiled into Figure 6d. The figure illustrates that at the 10 mg/kg dose, nearly all the iron introduced via PUSIONPs remained within the body, with the majority being utilized for

hemoglobin synthesis. However, as the dose increased, the proportion of iron entering hemoglobin gradually decreased. Additionally, the total iron retained in the body diminished with higher doses, suggesting that at elevated dosages, once the body's iron requirements are met, the IDA rat gradually metabolizes and excretes the excess iron through normal iron metabolism pathways to restore iron homeostasis.

2.8. Biosafety Assessment of PUSIONPs. The preceding results indicate that following intravenous administration, PUSIONPs primarily accumulate in the liver and spleen, where they gradually degrade and integrate into the body's iron metabolism. To evaluate whether PUSIONPs might pose any biosafety concerns during this process, *in vitro* cytotoxicity was evaluated using the cell counting kit-8 (CCK-8) assay and an apoptotic assay in HepG2 cells, a widely recognized model for toxicity studies due to its retention of key liver functions.⁶⁴ The results demonstrated no significant cytotoxicity, as shown in Figures S15 and S16. Furthermore, a hemolysis assay was conducted to assess the hemolytic potential of PUSIONPs (Figure S17). Even at a high concentration of 1000 $\mu\text{g}/\text{mL}$, the hemolysis rate remained well below the internationally accepted threshold of 5%, indicating that PUSIONPs exhibited no apparent hemolytic activity.

To further evaluate biosafety *in vivo*, several key parameters were assessed in both normal and IDA rats at different time points following administration at a dose of 20 mg/kg. Given the potential toxicity associated with excess iron released from

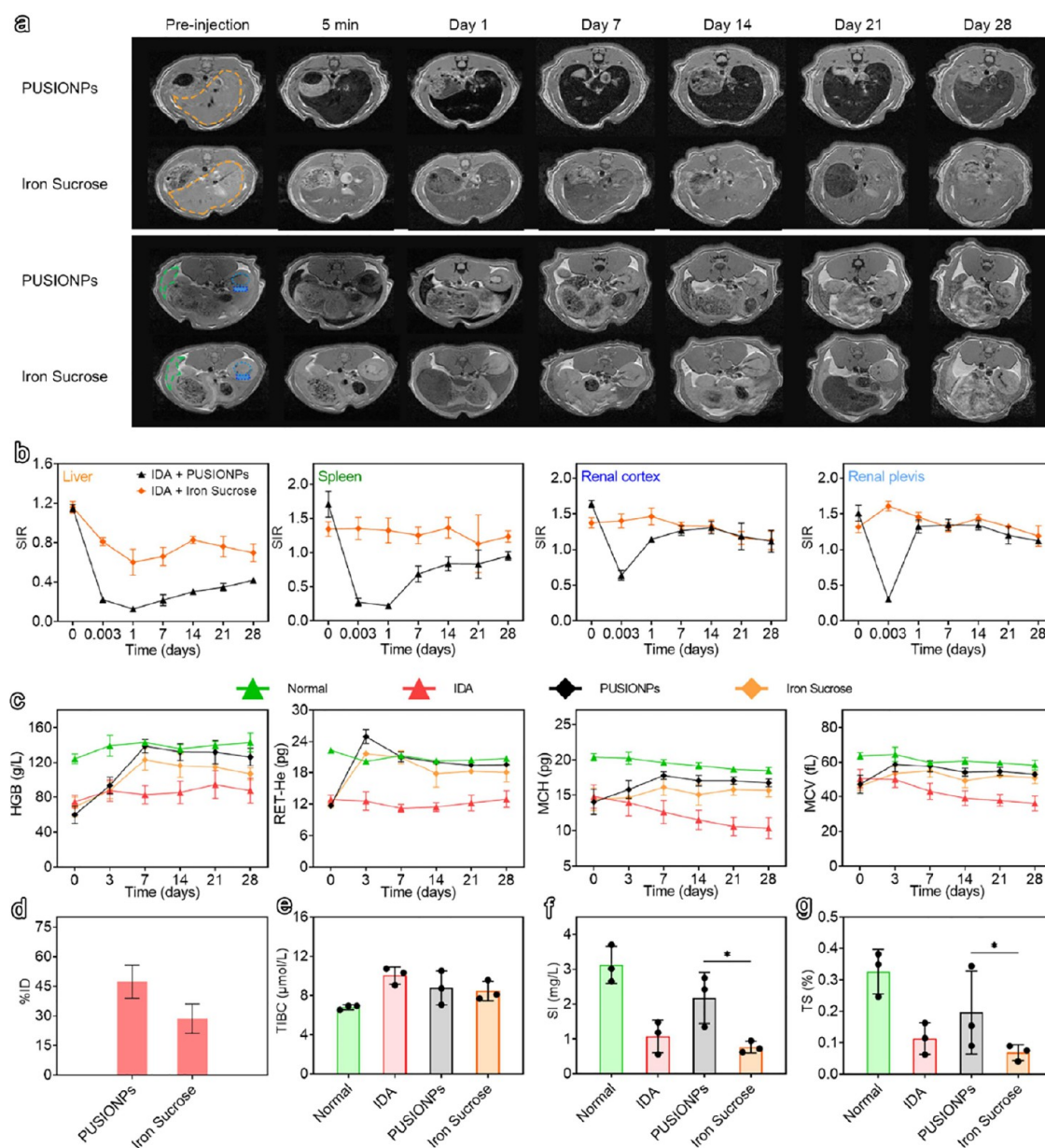


Figure 8. Comparative study of iron supplementation effects between PUSIONPs and iron sucrose at a dose of 40 mg/kg. (a) T1-weighted MRI images showing biodistribution of PUSIONPs and iron sucrose at various time points postinjection. (b) SIR changes over time in different organs, including liver, spleen, renal cortex, and renal pelvis. $n = 4$ rats per group (c) Trends in hemoglobin (HGB), reticulocyte hemoglobin equivalent (RET-He), mean corpuscular hemoglobin (MCH), mean corpuscular volume (MCV) after injection. (d) Percentage of injected iron incorporated into hemoglobin, (e) total iron-binding capacity (TIBC), (f) serum iron (SI), and (g) transferrin saturation (TS) measured 28 days after administration. Data are presented as mean \pm SD, $n = 4$ rats per group.

PUSIONPs, oxidative stress-related parameters were measured in the liver (Figure 7a) and serum (Figure 7b). The increase in malondialdehyde (MDA) levels in the liver of both normal and IDA rats suggested the possibility of lipid peroxidation. However, the concurrent rise in glutathione (GSH) levels and the stable levels of superoxide dismutase (SOD) indicated an activated antioxidant response. Notably, the increases in MDA and GSH were more pronounced in the livers of normal rats compared to IDA rats. This difference is likely because, in IDA rats, the iron released from PUSIONPs is rapidly transferred to the hematopoietic system for hemoglobin synthesis, thereby reducing the iron burden on the liver. Despite these findings, which suggest that PUSIONPs degradation might induce oxidative stress, the body's

simultaneous activation of antioxidant defenses appears to mitigate this effect, ensuring that the process does not pose a biosafety risk. Moreover, no significant changes in oxidative stress-related parameters were observed in the serum, indicating minimal levels of free iron in the bloodstream.

In addition, serum biochemical indicators related to hepatic and renal toxicity were assessed (Figure 7c). Although some fluctuations were observed over time, all parameters remained within normal ranges, with most showing no significant differences compared to preadministration levels. These results further suggest that PUSIONPs at this dose do not pose a safety risk. Histological examinations of major organs revealed no pronounced inflammatory, dystrophic, or necrotic changes

in tissues stained with hematoxylin-eosin (Figure S18), further confirming the safety of PUSIONPs.

Finally, blood biochemical parameters were tested in IDA rats 28 days after administration at different doses, as shown in Figure S19. All values remained within normal ranges, with no apparent dose-dependent effects, indicating no toxicity. Therefore, the safe profile of PUSIONPs, coupled with their regulation of iron homeostasis, establishes a strong foundation for their use in various biomedical applications.

2.9. PUSIONPs for Intravenous Iron Therapy in Iron Deficiency Anemia. To evaluate the efficacy of PUSIONPs as an intravenous iron therapy for treating IDA, their performance was compared with that of iron sucrose, a commonly used intravenous iron supplement. Both treatments were administered at a dose of 40 mg Fe/kg body weight. Figures 8a and S20a present representative T1- and T2-weighted MR images taken at various time points post-injection. The corresponding quantitative analyses of the SIR and T2* values are provided in Figures 8b, S20b, and S21. The imaging results indicate that iron sucrose exhibited a different imaging profile compared to PUSIONPs. Although iron sucrose, like PUSIONPs, was primarily taken up by the liver and spleen,⁵⁵ its nonsuperparamagnetic nature resulted in less pronounced changes in MRI signals compared to PUSIONPs. However, the quantitative MRI results show that iron sucrose was metabolized more rapidly in the liver and spleen, with faster signal recovery observed in these organs.

Despite these differences, the hematological parameters measured postinjection (Figure 8c) indicate that both PUSIONPs and iron sucrose effectively increased HGB levels in IDA rats. Notably, PUSIONPs demonstrated a more consistent and sustained increase in HGB over time. Improvements were also observed in the RET-He, MCH, and MCV, with PUSIONPs yielding higher levels in all these parameters. This suggests that PUSIONPs facilitate more efficient erythropoiesis and iron utilization compared to iron sucrose.

Figure 8d quantifies the percentage of injected iron incorporated into hemoglobin after 28 days. The results show that PUSIONPs led to higher iron incorporation into hemoglobin than iron sucrose, indicating superior bioavailability and utilization of the administered iron. The slower clearance of PUSIONPs from major organs such as the liver and spleen likely contributed to the pronounced elevation in hemoglobin levels, demonstrating the potential of PUSIONPs as a more effective treatment for IDA. Additionally, as shown in Figure 8e–g, PUSIONPs exhibited a relatively more favorable profile in total iron-binding capacity (TIBC), serum iron (SI), and transferrin saturation (TS), with these parameters closer to normal levels. This suggests that PUSIONPs can more effectively restore balanced iron status.

The MRI tracking data, combined with the hematological and serum iron measurements, suggest that PUSIONPs provide a more sustained and efficient iron delivery system compared to iron sucrose. Moreover, the ability of PUSIONPs to maintain a stable iron profile in serum without causing iron overload further supports their safety and efficacy in iron supplementation therapy. These findings pave the way for future studies to explore the clinical application of PUSIONPs in treating human iron deficiency and related disorders.

3. CONCLUSIONS

This study provides a comprehensive understanding of the pivotal role that iron homeostasis plays in the *in vivo* degradation and transformation of iron oxide nanoparticles, specifically PUSIONPs. Our findings demonstrate that under iron-deficient conditions, PUSIONPs degrade more rapidly, with the resulting iron swiftly incorporated into hemoglobin, underscoring the body's capacity to regulate PUSIONPs metabolism in response to varying physiological needs. Moreover, the liver and spleen, owing to their distinct physiological functions, displayed differential rates and pathways of PUSIONP metabolism. The spleen, primarily responsible for iron recycling and utilization, facilitated a faster degradation of PUSIONPs compared to the liver, which functions predominantly as an iron storage organ. In iron-deficient states, the majority of degradation products from both the liver and spleen were efficiently channeled into the hematopoietic system for hemoglobin synthesis, with minimal excretion from the body. Conversely, under normal iron balance, the ferritin produced from PUSIONPs degradation in the liver was stored and gradually metabolized out through standard iron metabolism pathways, while in the spleen, ferritin accumulation was more pronounced due to the additional recycling of iron from aging red blood cells. This suggests that the spleen may serve as a key target organ for PUSIONPs.

The degradation behavior of PUSIONPs also demonstrated a clear dose dependency. At lower doses under iron-deficient conditions, PUSIONPs were predominantly taken up by the liver and spleen, rapidly degraded, and utilized for hemoglobin synthesis. At higher doses, the body modulated the degradation and metabolism of PUSIONPs based on the restoration of iron homeostasis, with initial degradation products supporting hemoglobin synthesis, and excess iron gradually being metabolized out once balance was achieved. Furthermore, safety assessments across the studied dose range confirmed the excellent biocompatibility of PUSIONPs. Compared to the clinically used intravenous iron supplement, iron sucrose, PUSIONPs showed superior bioavailability and more efficient iron supplementation. These findings not only enhance our understanding of the interaction between iron oxide nanoparticles and the body's iron regulatory mechanisms but also lay the groundwork for future research exploring the potential of PUSIONPs in various clinical applications.

4. EXPERIMENT SECTION

4.1. Characterization. TEM images were captured using a Talos F200S G2 transmission electron microscope operating at an acceleration voltage of 200 kV. The hydrodynamic size and Zeta potential were measured at 25 °C with a Malvern Zeta sizer Nano ZS90 equipped with a solid state He–Ne laser ($\lambda = 633$ nm). The iron concentration of PUSIONPs was determined by the 1,10-phenanthroline spectrophotometric method after the resulting nanoparticles were digested by HCl. In all experiments, the concentration of PUSIONPs was defined by the content of iron. The relaxivity measurements were carried out on a 3 T preclinical MRI instrument (MRS300, MR Solutions). Ultraviolet–Visible absorption spectrum was recorded on a Shimadzu UV–vis spectrophotometer UV-3600 using quartz cuvettes with an optical path of 1 cm. Representative photomicrographs were taken by an Olympus FV 1200 laser scanning confocal microscope.

4.2. Relaxivity Measurement of PUSIONPs. To measure the relaxivities (r_1 and r_2) of PUSIONPs, a series of solutions with varying PUSIONPs concentrations were prepared. For the determination of the longitudinal relaxation time (T_1), an inversion recovery fast low-angle shot (IR FLASH) sequence was utilized. T_1 values were obtained by analyzing MRI images acquired with varying repetition times (TR) ranging from 90 to 10,000 ms, while keeping the echo time (TE) constant at 10 ms. To determine the transverse relaxation time (T_2), a multiecho multislice (MEMS) sequence was employed, with T_2 values obtained by varying TE values from 15 to 450 ms, while maintaining a constant TR of 1400 ms. The relaxivities r_1 and r_2 were calculated by determining the slope of the curve for longitudinal relaxation rate ($1/T_1$, R_1) and transverse relaxation rate ($1/T_2$, R_2) plotted against the molar iron concentration.

4.3. Animals. All animal procedures were conducted in accordance with guidelines approved by the Ethics Committee of Soochow University (Soochow, China). Specific pathogen-free (SPF) grade male Sprague–Dawley (SD) rats, weighing 80–100 g, were obtained from Changzhou Cavens Company. The animals were housed in the SPF animal facility of Soochow University, maintained at 25 °C with a 12-h light/dark cycle.

To develop the IDA rat model, three-week-old male SD rats were fed a low-iron diet containing approximately 5 mg Fe/kg for 3–4 weeks. Blood samples were collected weekly from the retro-orbital sinus to monitor hematological parameters using a hematology analyzer (XY-1000-B1, Sysmex). IDA was confirmed when hemoglobin levels fell below 100 g/L. Throughout the study, IDA rats were continuously maintained on a low-iron diet, while the control rats were provided with a standard diet containing approximately 200 mg Fe/kg. All rats were given deionized water during the study.

4.4. In Vivo MR Imaging. Rats were anesthetized with 4–5% isoflurane in oxygen for induction and maintained at 1–2% isoflurane during imaging. MR images were acquired using respiratory gating on a 3 T preclinical MRI system (MRS300, MR Solutions) with a rat body coil. T1-weighted images were acquired using an FSE sequence with parameters set at TR/TE = 1723/11 ms, matrix size = 256 × 256, FOV = 60 × 60 mm², and slice thickness = 1.0 mm. Similarly, T2-weighted images were acquired using an FSE sequence with parameters set at TR/TE = 4573/68 ms, matrix size = 256 × 256, FOV = 60 × 60 mm², and slice thickness = 1.0 mm. Quantitative T2* images were obtained using a multigradient echo (MGE) sequence with TR = 600 ms, TE = 3.5–31.4 ms, flip angle = 20°, matrix size = 256 × 256, FOV = 60 × 60 mm², and slice thickness = 1.0 mm. Imaging was performed before PUSIONPs injection and at 5 min, 1 day, 7 days, 14 days, 21 days, and 28 days postinjection.

Signal intensity (SI) in the liver, spleen, renal cortex, renal pelvis, and paraspinal muscles was measured before and after PUSIONPs injection. Regions of interest (ROIs) were drawn in the same areas for consistency. The signal intensity ratio (SIR) of all T2-weighted and T1-weighted images was calculated using the following equation: $SIR = SI/SI_m$, where SI represents the signal intensity in the ROIs of the liver, spleen, renal cortex, and renal pelvis, and SI_m represents the signal intensity in the ROIs of the paraspinal muscles in the same slice. T2* values for each ROI were postprocessed in Preclinical Scan software (MRS300, MR Solutions). At least three slices per rat were analyzed.

4.5. Iron Content Analysis in Tissues. The animals were anesthetized with 1–2% isoflurane mixed with oxygen, followed by transcardial perfusion with cold saline to collect liver, spleen, kidney, heart, lung, and brain tissues at various time points after PUSIONPs injection. The collected organs were weighed and then lyophilized prior to analysis. The iron concentration in these tissues was determined using inductively coupled plasma optical emission spectrometry (ICP-OES, ICAP7200, Thermo) after acid digestion.

4.6. Iron Content Analysis in Urine and Feces. The animals were housed in metabolic cages designed to separate urine and feces for collection over a 28-day period. Each cage was equipped with two inlets (one for water and one for food) and two outlets (one for urine and one for feces), ensuring clean and separate sample collection. The feces were dried to a constant weight, and both urine and feces samples were digested and analyzed for iron content using ICP-OES (ICAP7200, Thermo).

4.7. Histology Analysis. For histological analysis, the animals were anesthetized with 1–2% isoflurane in oxygen, followed by transcardial perfusion with cold saline to collect the liver, spleen, kidney, heart, lung, and brain at various time points post-PUSIONPs injection. Portions of each organ were isolated and fixed in 4% paraformaldehyde solution. The fixed tissues were then embedded in paraffin, sectioned into 4 μm thick slices, and stained with Prussian blue or hematoxylin and eosin. Specific primary antibodies, including FTL, TFR and FPN were used for immunohistochemical staining. The stained sections were examined under an optical microscope (MF52-N, MSHOT).

4.8. Hematological Analysis. Blood samples were collected from the retro-orbital sinus for hematological analysis before the start of the experiment and at 7, 14, 21, and 28 day postinjection. Prior to each blood collection, the rats were anesthetized with 4–5% isoflurane in oxygen. Approximately 200 μL of blood was collected at each time point and analyzed for hematological parameters using a hematology analyzer (XY-1000-B1, Sysmex).

4.9. Blood Biochemistry Analysis. Blood samples were collected from the retro-orbital sinus for biochemical analysis before the experiment and at various time points postinjection. To obtain serum, the blood samples were incubated at room temperature for 30 min, followed by centrifugation at 1800 g for 15 min. The resulting serum was then analyzed for aminotransferase (ALT), aspartate aminotransferase (AST), alkaline phosphatase (ALP), urea (UREA), creatinine (CREA), and γ -glutamyl transpeptidase (GGT) levels using an ADVIA 2120i analyzer (Siemens).

4.10. Western Blot. Liver and spleen tissues were collected before the experiment and at 1, 7, 28 days postinjection. The tissues were lysed using RIPA lysis buffer supplemented with a protease and phosphatase inhibitor cocktail (P1050, Beyotime). The extracted proteins were separated by SDS-polyacrylamide gel electrophoresis (SDS-PAGE) and subsequently transferred onto polyvinylidene difluoride (PVDF) membranes. The membranes were blocked for 60 min and then incubated overnight at 4 °C with primary antibodies, including GAPDH mouse antibody (1:50,000, Proteintech), antitransferrin receptor antibody (1:5000, Abcam), anti-SLC40A1 antibody (1:5000, Abcam) and anti-FTL antibody (1:5000, Abcam). Following primary antibody incubation, the membranes were treated with HRP-labeled Goat Anti-Mouse IgG (H+L) (1:500, Beyotime) and HRP-labeled Goat Anti-

Rabbit IgG (H+L) (1:500, Beyotime) for 60 min at room temperature. The protein bands were visualized and imaged using a FluorChem M imaging system.

4.11. Oxidative Stress Analysis. The malondialdehyde (MDA) content in liver and serum was quantified using a thiobarbituric acid assay kit (A003-1-2, Nanjing Jiancheng Bioengineering Institute). The absorbance at 532 nm was measured using a spectrophotometer, with 1,1,3,3-tetramethoxypropane serving as an external standard. Superoxide dismutase (SOD) activity in liver and serum was assessed using Xanthine Oxidase Assay Kits (A001-3-2, Nanjing Jiancheng Bioengineering Institute). Glutathione (GSH) levels in liver and serum were determined by an assay based on the conjugation of GSH with 5,5'-Dithiobis (2-nitrobenzoic acid) [DTNB], also sourced from Nanjing Jiancheng Bioengineering Institute, China.

4.12. Cytotoxicity Assay. Cytotoxicity assays were performed using HepG2 cells at 37 °C under 5% CO₂. HepG2 cells were seeded in 96-well plates for 12 h. Then, PUSIONPs at the indicated concentrations (0, 2, 10, 20, 50, 100, 200, 500 μg/mL), were added to the cell culture medium. The cells were then incubated with PUSIONPs for an additional 24 h. To assess toxicity, 100 μL of cell culture medium containing 10 μL CCK-8 solution (K1018, APEX BIO) was added to each well of the 96-well plate and the plate was incubated in the CO₂ incubator for additional 2 h. Enzyme dehydrogenase in living cells was oxidized by this kit to orange carapace. The quality of this product was assessed calorimetrically by using spectrophotometer with measurements based on absorbance values at 450 nm.

4.13. Cell Apoptotic Analysis. Cell apoptotic analysis was conducted by Annexin V-FITC/PI Apoptosis Kit (E-CK-A211, Elabscience) using HepG2 cells at 37 °C under 5% CO₂. The cells were seeded in a 6-well plate and cultured overnight. Subsequently, the cells were treated with PUSIONPs (100 μg/mL) for 24 h. The collected cells were dispersed with 100 μL 1× binding buffer, and then, they were incubated with 5 μL Annexin V-FITC and 5 μL PI staining solution for 15 min at room temperature in the dark. The stained cells were detected by a Beckman CytoFLEX Flow Cytometer.

4.14. Hemolysis Assay. Rat RBCs were carefully washed multiple times with PBS to ensure high quality. PBS were added to RBCs to obtain a 4% diluted RBC suspension. In a 1.5 mL tube, 500 μL of PUSIONPs with different concentrations (0, 50, 100, 200, 400 μg/mL) was combined with 500 μL of the 4% RBC suspension and 4% RBC supernatant, respectively. The mixture was incubated at 37 °C for 1 h. Positive and negative controls were conducted using DI water and PBS only, respectively. Following incubation, the solutions were centrifuged at 3000 rpm for 15 min. Subsequently, the supernatant was transferred to a 96-well plate to measure the absorbance at 540 nm. The hemolysis rate was calculated using the following formula:

$$\text{Hemolysis (\%)} = \frac{(\text{OD}_T - \text{OD}_{TC} - \text{OD}_{NC})}{(\text{OD}_{PC} - \text{OD}_{NC})} \times 100\%$$

OD_T = absorbance value of the samples of interest; OD_{TC} = absorbance value of the samples control; OD_{NC} = absorbance value of the negative control; OD_{PC} = absorbance value of the positive control.

4.15. Statistical Analysis. All data are presented as means ± SD. Statistical differences were analyzed using an unpaired

Student's *t* test. Statistical significance is indicated in the figures as follows: ****P* < 0.001, ***P* < 0.01, **P* < 0.05.

ASSOCIATED CONTENT

Supporting Information

The Supporting Information is available free of charge at <https://pubs.acs.org/doi/10.1021/acsnano.5c01399>.

Characterization and MR property evaluation of PUSIONPs; hematological parameters of IDA model; SI of T₂-weighted and T₁-weighted MR images of PUSIONPs in normal and IDA rats; quantitative T₂* changes of PUSIONPs in normal and IDA rats; PB staining of liver, lung, heart and brain after the intravenous injection of PUSIONPs in normal and IDA rats; changes in HGB and RET-He levels over 7 days following the injection of PUSIONPs; analysis of iron content in urine and feces after PUSIONPs injection; FTL, TFR and FPN staining of liver and spleen; representative T₂-weighted MR images, signal intensity ratio and quantitative T₂* changes following PUSIONPs injection at different doses; PB staining of PUSIONPs at different doses; distribution of PUSIONPs with different doses; relative viability, cell apoptosis and hemolytic property of PUSIONPs; H&E staining and biochemical parameters postinjection of PUSIONPs; and T₂-weighted MR images, signal intensity ratio and quantitative T₂* changes following PUSIONPs and iron sucrose injection (PDF)

AUTHOR INFORMATION

Corresponding Authors

Jianfeng Zeng – Center for Molecular Imaging and Nuclear Medicine, State Key Laboratory of Radiation Medicine and Protection, School for Radiological and Interdisciplinary Sciences (RAD-X), Collaborative Innovation Center of Radiological Medicine of Jiangsu Higher Education Institutions, Soochow University, Suzhou 215123, China; orcid.org/0000-0001-7654-8724; Email: jfzeng@suda.edu.cn

Mingyuan Gao – Center for Molecular Imaging and Nuclear Medicine, State Key Laboratory of Radiation Medicine and Protection, School for Radiological and Interdisciplinary Sciences (RAD-X), Collaborative Innovation Center of Radiological Medicine of Jiangsu Higher Education Institutions and School of Life Sciences, Soochow University, Suzhou 215123, China; The Second Affiliated Hospital of Soochow University, Suzhou 215123, China; orcid.org/0000-0002-7360-3684; Email: gaomy@suda.edu.cn

Authors

Ning Wang – Center for Molecular Imaging and Nuclear Medicine, State Key Laboratory of Radiation Medicine and Protection, School for Radiological and Interdisciplinary Sciences (RAD-X), Collaborative Innovation Center of Radiological Medicine of Jiangsu Higher Education Institutions, Soochow University, Suzhou 215123, China

Dandan Zhou – Center for Molecular Imaging and Nuclear Medicine, State Key Laboratory of Radiation Medicine and Protection, School for Radiological and Interdisciplinary Sciences (RAD-X), Collaborative Innovation Center of Radiological Medicine of Jiangsu Higher Education

Institutions, Soochow University, Suzhou 215123, China;

orcid.org/0000-0002-7054-4498

Keyang Xu – Center for Molecular Imaging and Nuclear Medicine, State Key Laboratory of Radiation Medicine and Protection, School for Radiological and Interdisciplinary Sciences (RAD-X), Collaborative Innovation Center of Radiological Medicine of Jiangsu Higher Education Institutions, Soochow University, Suzhou 215123, China

Dandan Kou – Center for Molecular Imaging and Nuclear Medicine, State Key Laboratory of Radiation Medicine and Protection, School for Radiological and Interdisciplinary Sciences (RAD-X), Collaborative Innovation Center of Radiological Medicine of Jiangsu Higher Education Institutions, Soochow University, Suzhou 215123, China

Can Chen – Center for Molecular Imaging and Nuclear Medicine, State Key Laboratory of Radiation Medicine and Protection, School for Radiological and Interdisciplinary Sciences (RAD-X), Collaborative Innovation Center of Radiological Medicine of Jiangsu Higher Education Institutions, Soochow University, Suzhou 215123, China

Cang Li – Center for Molecular Imaging and Nuclear Medicine, State Key Laboratory of Radiation Medicine and Protection, School for Radiological and Interdisciplinary Sciences (RAD-X), Collaborative Innovation Center of Radiological Medicine of Jiangsu Higher Education Institutions, Soochow University, Suzhou 215123, China

Jianxian Ge – Center for Molecular Imaging and Nuclear Medicine, State Key Laboratory of Radiation Medicine and Protection, School for Radiological and Interdisciplinary Sciences (RAD-X), Collaborative Innovation Center of Radiological Medicine of Jiangsu Higher Education Institutions, Soochow University, Suzhou 215123, China

Lei Chen – Center for Molecular Imaging and Nuclear Medicine, State Key Laboratory of Radiation Medicine and Protection, School for Radiological and Interdisciplinary Sciences (RAD-X), Collaborative Innovation Center of Radiological Medicine of Jiangsu Higher Education Institutions, Soochow University, Suzhou 215123, China

Complete contact information is available at:

<https://pubs.acs.org/10.1021/acsnano.5c01399>

Author Contributions

The manuscript was written through contributions of all authors. All authors have given approval to the final version of the manuscript.

Notes

The authors declare no competing financial interest.

ACKNOWLEDGMENTS

This research was funded by the National Natural Science Foundation of China (82130059, 82222033, 82172003), the National Key Research and Development Program of China (2018YFA0208800), and the Priority Academic Program Development of Jiangsu Higher Education Institutions (PAPD).

REFERENCES

(1) Si, G.; Du, Y.; Tang, P.; Ma, G.; Jia, Z.; Zhou, X.; Mu, D.; Shen, Y.; Lu, Y.; Mao, Y.; et al. Unveiling the next generation of MRI contrast agents: current insights and perspectives on ferumoxytol-enhanced MRI. *Natl. Sci. Rev.* **2024**, *11* (5), No. nwa057.

(2) Vasić, K.; Knez, Ž.; Leitgeb, M. Multifunctional Iron Oxide Nanoparticles as Promising Magnetic Biomaterials in Drug Delivery: A Review. *J. Funct. Biomater.* **2024**, *15* (8), 227.

(3) Kacem, M.; Essoumhi, A.; Dib, M. Magnetic iron oxide-based materials and their hyperthermia application: A review. *Inorg. Chem. Commun.* **2024**, *166*, No. 112510.

(4) Lu, M.; Cohen, M. H.; Rieves, D.; Pazdur, R. FDA report: Ferumoxytol for intravenous iron therapy in adult patients with chronic kidney disease. *Am. J. Hematol.* **2010**, *85* (5), 315–319.

(5) Zhang, T. G.; Miao, C. Y. Iron Oxide Nanoparticles as Promising Antibacterial Agents of New Generation. *Nanomaterials (Basel)* **2024**, *14* (15), 1311.

(6) Fan, Q.; Xiong, W.; Zhou, H.; Yang, J.; Feng, J.; Li, Z.; Wu, L.; Hu, F.; Duan, X.; Li, B. An AND Logic Gate for Magnetic-Resonance-Imaging-Guided Ferroptosis Therapy of Tumors. *Adv. Mater.* **2023**, *35* (45), No. e2305932.

(7) Sukhbaatar, N.; Weichhart, T. Iron Regulation: Macrophages in Control. *Pharmaceuticals (Basel)* **2018**, *11* (4), 137.

(8) Dev, S.; Babitt, J. L. Overview of iron metabolism in health and disease. *Hemodial Int.* **2017**, *21* (Suppl. 1), S6–s20.

(9) Papanikolaou, G.; Pantopoulos, K. Iron metabolism and toxicity. *Toxicol. Appl. Pharmacol.* **2005**, *202* (2), 199–211.

(10) Dixon, S. J.; Stockwell, B. R. The role of iron and reactive oxygen species in cell death. *Nat. Chem. Biol.* **2014**, *10* (1), 9–17.

(11) Dixon, S. J.; Olzmann, J. A. The cell biology of ferroptosis. *Nat. Rev. Mol. Cell Biol.* **2024**, *25* (6), 424–442.

(12) Stockwell, B. R. Ferroptosis turns 10: Emerging mechanisms, physiological functions, and therapeutic applications. *Cell* **2022**, *185* (14), 2401–2421.

(13) Ru, Q.; Li, Y.; Chen, L.; Wu, Y.; Min, J.; Wang, F. Iron homeostasis and ferroptosis in human diseases: mechanisms and therapeutic prospects. *Signal Transduct Target Ther.* **2024**, *9* (1), 271.

(14) Ganz, T. Systemic iron homeostasis. *Physiol Rev.* **2013**, *93* (4), 1721–1741.

(15) Weissleder, R.; Stark, D. D.; Engelstad, B. L.; Bacon, B. R.; Compton, C. C.; White, D. L.; Jacobs, P.; Lewis, J. Superparamagnetic iron oxide: pharmacokinetics and toxicity. *AJR Am. J. Roentgenol* **1989**, *152* (1), 167–173.

(16) Bourrinet, P.; Bengel, H. H.; Bonnemain, B.; Dencausse, A.; Idee, J. M.; Jacobs, P. M.; Lewis, J. M. Preclinical safety and pharmacokinetic profile of ferumoxtran-10, an ultrasmall superparamagnetic iron oxide magnetic resonance contrast agent. *Invest Radiol* **2006**, *41* (3), 313–324.

(17) Lartigue, L.; Alloyeau, D.; Kolosnjaj-Tabi, J.; Javed, Y.; Guardia, P.; Riedinger, A.; Péchoux, C.; Pellegrino, T.; Wilhelm, C.; Gazeau, F. Biodegradation of iron oxide nanocubes: high-resolution in situ monitoring. *ACS Nano* **2013**, *7* (5), 3939–3952.

(18) Levy, M.; Luciani, N.; Alloyeau, D.; Elgrabli, D.; Deveaux, V.; Pechoux, C.; Chat, S.; Wang, G.; Vats, N.; Gendron, F.; et al. Long term in vivo biotransformation of iron oxide nanoparticles. *Biomaterials* **2011**, *32* (16), 3988–3999.

(19) Javed, Y.; Lartigue, L.; Hugounenq, P.; Vuong, Q. L.; Gossuin, Y.; Bazzi, R.; Wilhelm, C.; Ricolleau, C.; Gazeau, F.; Alloyeau, D. Biodegradation mechanisms of iron oxide monocrystalline nanoflowers and tunable shield effect of gold coating. *Small* **2014**, *10* (16), 3325–3337.

(20) Gao, J.; Zhou, H.; Zhao, Y.; Lu, L.; Zhang, J.; Cheng, W.; Song, X.; Zheng, Y.; Chen, C.; Tang, J. Time-course effect of ultrasmall superparamagnetic iron oxide nanoparticles on intracellular iron metabolism and ferroptosis activation. *Nanotoxicology* **2021**, *15* (3), 366–379.

(21) Gu, J.; Xu, H.; Han, Y.; Dai, W.; Hao, W.; Wang, C.; Gu, N.; Xu, H.; Cao, J. The internalization pathway, metabolic fate and biological effect of superparamagnetic iron oxide nanoparticles in the macrophage-like RAW264.7 cell. *Sci China. Life Sci.* **2011**, *54* (9), 793–805.

(22) Rojas, J. M.; Sanz-Ortega, L.; Mulens-Arias, V.; Gutierrez, L.; Perez-Yague, S.; Barber, D. F. Superparamagnetic iron oxide nanoparticle uptake alters M2 macrophage phenotype, iron

- metabolism, migration and invasion. *Nanomedicine* **2016**, *12* (4), 1127–1138.
- (23) Rouault, T. A.; Klausner, R. D. Post-transcriptional regulation of genes of iron metabolism in mammalian cells. *JBIC Journal of Biological Inorganic Chemistry* **1996**, *1* (6), 494–499.
- (24) Zhou, Z. D.; Tan, E. K. Iron regulatory protein (IRP)-iron responsive element (IRE) signaling pathway in human neurodegenerative diseases. *Mol. Neurodegener.* **2017**, *12* (1), 75.
- (25) Sebastiani, G.; Wilkinson, N.; Pantopoulos, K. Pharmacological Targeting of the Hcpicidin/Ferroportin Axis. *Front Pharmacol.* **2016**, *7*, 160.
- (26) Wang, L.; Cherayil, B. J. Ironing out the wrinkles in host defense: interactions between iron homeostasis and innate immunity. *J. Innate Immun* **2009**, *1* (5), 455–464.
- (27) McLean, E.; Cogswell, M.; Egli, I.; Wojdyla, D.; de Benoist, B. Worldwide prevalence of anaemia, WHO Vitamin and Mineral Nutrition Information System, 1993–2005. *Public Health Nutr* **2009**, *12* (4), 444–454.
- (28) Camaschella, C. Iron deficiency [Erratum in Blood 2019;133(1):30–39]. *Blood* **2023**, *141* (6), 682.
- (29) Bjørnerud, A.; Johansson, L. O.; Ahlström, H. K. Pre-clinical results with Clariscan (NC100150 Injection): experience from different disease models. *Magma* **2001**, *12* (2–3), 99–103.
- (30) Daldrup-Link, H. E.; Kaiser, A.; Helbich, T.; Werner, M.; Bjørnerud, A.; Link, T. M.; Rummeny, E. J. Macromolecular contrast medium (feruglose) versus small molecular contrast medium (gadopentetate) enhanced magnetic resonance imaging: differentiation of benign and malignant breast lesions. *Acad. Radiol.* **2003**, *10* (11), 1237–1246.
- (31) Bentzen, L.; Vestergaard-Poulsen, P.; Nielsen, T.; Overgaard, J.; Bjørnerud, A.; Briley-Saebø, K.; Horsman, M. R.; Ostergaard, L. Intravascular contrast agent-enhanced MRI measuring contrast clearance and tumor blood volume and the effects of vascular modifiers in an experimental tumor. *Int. J. Radiat. Oncol. Biol. Phys.* **2005**, *61* (4), 1208–1215.
- (32) Bjørnerud, A.; Johansson, L. O.; Briley-Saebø, K.; Ahlström, H. K. Assessment of T1 and T2* effects in vivo and ex vivo using iron oxide nanoparticles in steady state—dependence on blood volume and water exchange. *Magn. Reson. Med.* **2002**, *47* (3), 461–471.
- (33) Arami, H.; Khandhar, A.; Liggitt, D.; Krishnan, K. M. In vivo delivery, pharmacokinetics, biodistribution and toxicity of iron oxide nanoparticles. *Chem. Soc. Rev.* **2015**, *44* (23), 8576–8607.
- (34) Wang, S.; Li, J.; Chen, L.; Zeng, J.; Gao, M. Fe²⁺-Dominated Relaxometric Properties of Iron Oxide Nanoparticles as MRI Contrast Agents. *J. Phys. Chem. Lett.* **2024**, *15* (34), 8861–8866.
- (35) Ge, J.; Chen, L.; Huang, B.; Gao, Y.; Zhou, D.; Zhou, Y.; Chen, C.; Wen, L.; Li, Q.; Zeng, J.; et al. Anchoring Group-Mediated Radiolabeling of Inorganic Nanoparticles—A Universal Method for Constructing Nuclear Medicine Imaging Nanoparticles. *ACS Appl. Mater. Interfaces* **2022**, *14* (7), 8838–8846.
- (36) Zhou, D.; Shan, S.; Chen, L.; Li, C.; Wang, H.; Lu, K.; Ge, J.; Wang, N.; Afshari, M. J.; Zhang, Y. Trapped in Endosome PEGylated Ultra-Small Iron Oxide Nanoparticles Enable Extraordinarily High MR Imaging Contrast for Hepatocellular Carcinomas. *Adv. Sci.* **2024**, *11* (39), No. e2401351.
- (37) Lu, K.; Zhang, R.; Wang, H.; Li, C.; Yang, Z.; Xu, K.; Cao, X.; Wang, N.; Cai, W.; Zeng, J.; et al. PEGylated Ultrasmall Iron Oxide Nanoparticles as MRI Contrast Agents for Vascular Imaging and Real-Time Monitoring. *ACS Nano* **2025**, *19* (3), 3519–3530.
- (38) Auerbach, M.; Macdougall, I. The available intravenous iron formulations: History, efficacy, and toxicology. *Hemodial. Int.* **2017**, *21* (S1), S83–S92.
- (39) Chen, B.; Sun, J.; Han, Y.; Gu, N. Research status and development trend of iron-based nano-medicine. *SCIENTIA SINICA Chimica* **2019**, *49* (9), 1156–1167.
- (40) Chen, C.; Li, Y.; Zhou, D.; Fan, J.; Hu, X.; Zhang, R.; Ge, J.; Cao, X.; Qi, H.; Wang, N.; et al. Splenic response to protein corona of nanoparticles in vivo. *Nano Today* **2025**, *62*, No. 102676.
- (41) Chaudhry, H. S.; Kasarla, M. R. *Microcytic Hypochromic Anemia*. In StatPearls, StatPearls Publishing Copyright © 2024, StatPearls Publishing LLC, 2024.
- (42) Peer, D.; Karp, J. M.; Hong, S.; Farokhzad, O. C.; Margalit, R.; Langer, R. Nanocarriers as an emerging platform for cancer therapy. *Nat. Nanotechnol* **2007**, *2* (12), 751–760.
- (43) Ferrari, M. Cancer nanotechnology: opportunities and challenges. *Nat. Rev. Cancer* **2005**, *5* (3), 161–171.
- (44) Wang, X.; Zhong, X.; Li, J.; Liu, Z.; Cheng, L. Inorganic nanomaterials with rapid clearance for biomedical applications. *Chem. Soc. Rev.* **2021**, *50* (15), 8669–8742.
- (45) Gandon, Y.; Olivie, D.; Guyader, D.; Aubé, C.; Oberti, F.; Sebillé, V.; Deugnier, Y. Non-invasive assessment of hepatic iron stores by MRI. *Lancet* **2004**, *363* (9406), 357–362.
- (46) Kuhlpeper, R.; Dahnke, H.; Matuszewski, L.; Persigehl, T.; von Wallbrunn, A.; Allkemper, T.; Heindel, W. L.; Schaeffter, T.; Bremer, C. R2 and R2* mapping for sensing cell-bound superparamagnetic nanoparticles: in vitro and murine in vivo testing. *Radiology* **2007**, *245* (2), 449–457.
- (47) Gneveckow, U.; Jordan, A.; Scholz, R.; Brüß, V.; Waldöfner, N.; Ricke, J.; Feussner, A.; Hildebrandt, B.; Rau, B.; Wust, P. Description and characterization of the novel hyperthermia- and thermoablation-system MFH 300F for clinical magnetic fluid hyperthermia. *Med. Phys.* **2004**, *31* (6), 1444–1451.
- (48) Kiessling, F.; Mertens, M. E.; Grimm, J.; Lammers, T. Nanoparticles for imaging: top or flop? *Radiology* **2014**, *273* (1), 10–28.
- (49) Kolosnjaj-Tabi, J.; Lartigue, L.; Javed, Y.; Luciani, N.; Pellegrino, T.; Wilhelm, C.; Alloyeau, D.; Gazeau, F. Biotransformations of magnetic nanoparticles in the body. *Nano Today* **2016**, *11* (3), 280–284.
- (50) Feliu, N.; Docter, D.; Heine, M.; Del Pino, P.; Ashraf, S.; Kolosnjaj-Tabi, J.; Macchiarini, P.; Nielsen, P.; Alloyeau, D.; Gazeau, F.; et al. In vivo degeneration and the fate of inorganic nanoparticles. *Chem. Soc. Rev.* **2016**, *45* (9), 2440–2457.
- (51) Hoekstra, L. T.; de Graaf, W.; Nibourg, G. A.; Heger, M.; Bennink, R. J.; Stieger, B.; van Gulik, T. M. Physiological and biochemical basis of clinical liver function tests: a review. *Ann. Surg* **2013**, *257* (1), 27–36.
- (52) Reddy, L. H.; Couvreur, P. Nanotechnology for therapy and imaging of liver diseases. *J. Hepatol* **2011**, *55* (6), 1461–1466.
- (53) Yang, Z.; Wu, S.; Gao, Y.; Kou, D.; Lu, K.; Chen, C.; Zhou, Y.; Zhou, D.; Chen, L.; Ge, J.; et al. Unveiling the Biologically Dynamic Degradation of Iron Oxide Nanoparticles via a Continuous Flow System. *Small Methods* **2024**, *8* (3), No. e2301479.
- (54) Han, J.; Tian, Y.; Wang, M.; Li, Y.; Yin, J.; Qu, W.; Yan, C.; Ding, R.; Guan, Y.; Wang, Q. Proteomics unite traditional toxicological assessment methods to evaluate the toxicity of iron oxide nanoparticles. *Front. Pharmacol.* **2022**, *13*, No. 1011065.
- (55) Brushmiller, J. G. Absorption and Malabsorption of Mineral Nutrients. Current Topics in Nutrition and Disease, Volume 12. Noel W. Solomons; Irwin H. Rosenberg; Anthony A. Albanese; David Kritchevsky. *Quarterly Review of Biology* **1985**, *60* (4), 559–559.
- (56) Ogawa, C.; Tsuchiya, K.; Maeda, K. Reticulocyte hemoglobin content. *Clin. Chim. Acta* **2020**, *504*, 138–145.
- (57) Bender, M. A.; Nielsen, K. R. Chapter 84—Hemoglobinopathies, 2011.
- (58) Yeo, J. H.; Colonne, C. K.; Tasneem, N.; Cosgriff, M. P.; Fraser, S. T. The iron islands: Erythroblastic islands and iron metabolism. *Biochim Biophys Acta Gen Subj* **2019**, *1863* (2), 466–471.
- (59) Levi, S.; Yewdall, S. J.; Harrison, P. M.; Santambrogio, P.; Cozzi, A.; Rovida, E.; Albertini, A.; Arosio, P. Evidence of H- and L-chains have co-operative roles in the iron-uptake mechanism of human ferritin. *Biochem. J.* **1992**, *288* (Pt2), 591–596.
- (60) Koorts, A. M.; Viljoen, M. Ferritin and ferritin isoforms II: protection against uncontrolled cellular proliferation, oxidative damage and inflammatory processes. *Arch Physiol Biochem* **2007**, *113* (2), 55–64.

(61) De Domenico, I.; Vaughn, M. B.; Li, L.; Bagley, D.; Musci, G.; Ward, D. M.; Kaplan, J. Ferroportin-mediated mobilization of ferritin iron precedes ferritin degradation by the proteasome. *Embo j* **2006**, *25* (22), 5396–5404.

(62) Beshara, S.; Lundqvist, H.; Sundin, J.; Lubberink, M.; Tolmachev, V.; Valind, S.; Antoni, G.; Långström, B.; Danielson, B. G. Pharmacokinetics and red cell utilization of iron(III) hydroxide-sucrose complex in anaemic patients: a study using positron emission tomography. *Br. J. Haematol.* **1999**, *104* (2), 296–302.

(63) Levy, M.; Lagarde, F.; Maraloiu, V. A.; Blanchin, M. G.; Gendron, F.; Wilhelm, C.; Gazeau, F. Degradability of superparamagnetic nanoparticles in a model of intracellular environment: follow-up of magnetic, structural and chemical properties. *Nanotechnology* **2010**, *21* (39), 395103.

(64) Guo, L.; Dial, S.; Shi, L.; Branham, W.; Liu, J.; Fang, J. L.; Green, B.; Deng, H.; Kaput, J.; Ning, B. Similarities and differences in the expression of drug-metabolizing enzymes between human hepatic cell lines and primary human hepatocytes. *Drug Metab. Dispos.* **2011**, *39* (3), 528–538.